Ana Claudia da Rocha

Final qualification work

Application of satellite imagery data for oil spills detection

Level of education: Master's degree
05.04.03 "Cartography and geoinformatics"
Educational program BM.5523.2020 "Geoinformation Cartography"

Supervisor:
Prof. Nico Giovanni PhD
Reviewer:
Researcher at St. Petersburg Mining University
Ponomarenko Maria Ruslanovna

2022

Saint Petersburg, 2022.

Ana Claudia da Rocha. MASTER'S DISSERTATION.
Institute of Earth Science,SPBU: SPB, 2022.

А.К. Да Роша — магстратура СПбГУ
e-mail: st018463@student.sbpu.ru А.К. Да Роша

Abstract

Attempting to corroborate to reduce the impact of oil spills, and to identify oil slicks and false alarms on the ocean surface, in a fast, effective and simple way, this paper studies targets on the surface of the ocean using Sentinel-1 data and "transect lines".

These lines traverse the image and offer the gray level value of each pixel they cross. The "state space," which is a mathematical space with orthogonal axes, has been chosen as the analytical instrument for this study. Such states will be presented as a spatially lagged diagram, i.e., a transect line will be plotted on the diagram in X and these same values will be lagged in space in the Y axis, defining the pair (DN(x), DN(x+k)), where k is an integer number of pixels.

Following the transect line, this will create a path-curve showing how the system changes as it goes through its states. Defining a signature to each k.

It has been confirmed that the trajectories created by the "sea," "oil," and "false alarm" systems in their lagged state-space diagrams exhibit diagnostic features.

Аннотация

В попытке помочь уменьшить последствия разливов нефти, а также быстро, эффективно и просто выявить нефтяные пятна и ложные цели на поверхности океана, в данной работе изучаются объекты на поверхности океана с помощью данных Sentinel-1 и "линий разрезов".

Эти линии пересекают изображение и указывают значение уровня серого для каждого пикселя, который они пересекают. В качестве аналитического инструмента для данного исследования было выбрано "пространство состояний", которое представляет собой математическое пространство с ортогональными осями. Такие состояния будут представлены в виде пространственно отложенной диаграммы, то есть на диаграмме будет проведена сквозная линия по оси X, и эти же значения будут отложены в пространстве по оси Y, определяя пару (DN(x), DN(x+k)), где k - целое число пикселей.

Следуя по линии разреза, можно построить кривую пути, показывающую, как изменяется система по мере прохождения состояний. Это определяет подпись для каждого k.

Было подтверждено, что траектории, созданные системами "море", "нефть" и "ложная цель" в их запаздывающих диаграммах пространства состояний, обладают диагностическими свойствами.

Table of Contents

Introduction

Remote sensing plays an increasingly vital role in spotting and responding rapidly to the oil spills location, allowing for more efficient planning of countermeasures (Fingas, 2016).

Synthetic aperture radar (SAR) is an active sensor that has been widely employed in satellites, and the detection of oil slicks using this radar is becoming an prevalent practice (Fingas, 2016). These sensors are active imaging devices that produce electromagnetic radiation in the microwave range and are thus unaffected by sunlight as well as the majority of weather conditions. SAR operates by the interaction of the electromagnetic wave with the target, followed by the collection of the backscatter by the sensor (Rebello, 2012).

The presence of oil in the water can be detected due to the surface roughness attenuation and the resulting reduction in backscattered signal; however, this process causes a series of ambiguities known as false alarms, since other events might induce similar attenuation (Bentz, 2006).

For the removal of false targets in the SAR image, manual procedures may be employed; however, this needs the crossover of a large number of data, such as in the work of Silva, (2009), in which information from the sea surface temperature, cloud top temperature, wind speed, wave height, and chlorophyll concentration is employed. Thus, the process of image interpretation is complicated, as it depends on the expertise of the interpreters and a variety of contextual information in addition to the radar picture.

Some works propose also the use of complex and heavy data and metodology to try to solve this problem, requiring very potent machines to process the data. (Song et al.,2020)

In this context, the current effort intends to collect data that validate the proposed methods for prospective automation of the detection of oil slicks and false targets in the water, making this recognition faster and less subjective.

Goals

Using a SENTINEL-1 image, the methodology proposes the use of lagged state diagrams for the identification of signatures that enable the ocean, oil slick, and fake target to be characterized (Silva et al., 2019). The purpose of this study is to provide evidence in support of the validity of the suggested approach and, as a result, to contribute to the acceleration of the oil and false alarms discrimination, that is necessary for the monitoring and accurate identification of oil slicks.

Purpose

The effects of oil spills along the coast, river estuaries, or low coastal regions can be disastrous. The amount of oil that is transported by sea every year surpasses 3 billion tons, which is higher than the total volume of commodities that are transported by water each year (Avalbaev & Kadirov, 2021). In addition, numerous minor slicks created by vessels might have negative effects on the coastal environment. In light of this circumstance, prompt detection of these leaks is essential.

Moreover, the actual potential of data collecting is far greater than our capability to process it, and the ability to extract the greatest amount of information from each type of data, without the need to use numerous distinct and heavy data to extract information, has a great value.

The purpose of this research attempting to identify oil slicks and false alarms on the ocean surface is to allow for a decrease in the time necessary for the location of oil spills, using the minimum amount of data, hence enabling speedier countermeasure preparation and preventing serious environmental concerns.

1. Literature review

1.1 Oil spill causes

Marine oil spills can have a great impact on natural environments and the main part of these accidents are associated with human activity. Large-scale oil spill accidents have a significant effect on the ocean environment for long periods of time. As an example, due the accident of Pyasino lake in 2020, more than 20,000 tons of diesel oil spilled into a river called the Ambarnaya which feeds into the Kara Sea, a part of the Arctic Ocean. This unfortunate accident contaminated not only the water bodies but also the surrounding subsoil (BBC News, 2020).

Constant monitoring of the water and oil spots on the ocean is extremely necessary. In the Baltic sea, one of the most trafficked seas in the world, every year around 120–140 accidents occur with an increase of 20% since 2006. The South-Eastern Baltic Sea is characterized by several oil spill hotspots, increasing the potential pollution risk for natural and socio-economic coastal resources (Depellegrin & Pereira, 2016).

It is interesting to notice that not only big accidents are the cause of this pollution, but also smaller licks from ships or improper disposal of oil in water may be the main cause. On the Black Sea, the chronic pollution due to frequent inputs of individually small oil volumes

released by marine traffic, tanker and off-shore operations, pipe-line seeps, and direct improper discharges is a greater threat to the coastal environment than a single catastrophic spill (Depellegrin & Pereira, 2016).

Not only human activity is the cause of the oil presence on the sea, but it can also happen due to natural conditions. The Marine exudation is the result of the natural escape of hydrocarbons (liquid or gaseous) directly from the source rock or reservoir. The oil and gas migrate through geological structures and permeable rocks to the bottom of the ocean (Macdonald et al., 1993). Usually, these exudations occur in small volumes and in events repeated over time. However, in the southern Gulf of Mexico these escapes occur continuously and in large volume, representing an environmental problem (Silva, 2009) (Bentz, 2006) and therefore have an extensive monitoring history.

Consequently, both accidental and natural oil spills can have social and environmental consequences that can be mitigated through fast monitoring.

1.2 Oil identification on the sea using remote sensing by satellite.

In the following paragraphs, basic information about oil identification by sensors onboard in satellites will be presented.

Taking into account the optical sensors, Fingas and Brown (2014) compiled information from different sources and presented them in a graphic that represents the characteristics of oil and water in distinct wavelengths (fig. 1, 2 and 3).

In the visible region of the electromagnetic spectrum, oil has a higher surface reflectance than water but does not show specific absorption/reflection tendencies. So overall, oil has no specific characteristics that distinguish it from the background (Brown et al., 2014).

Polarized lenses could be utilized as a potential solution to this issue. Oil could also be identified through the use of hyperspectral images; however, hyperspectral images are extremely complex and require advanced processing algorithms to meet near real-time application requirements (Li et al., 2021).

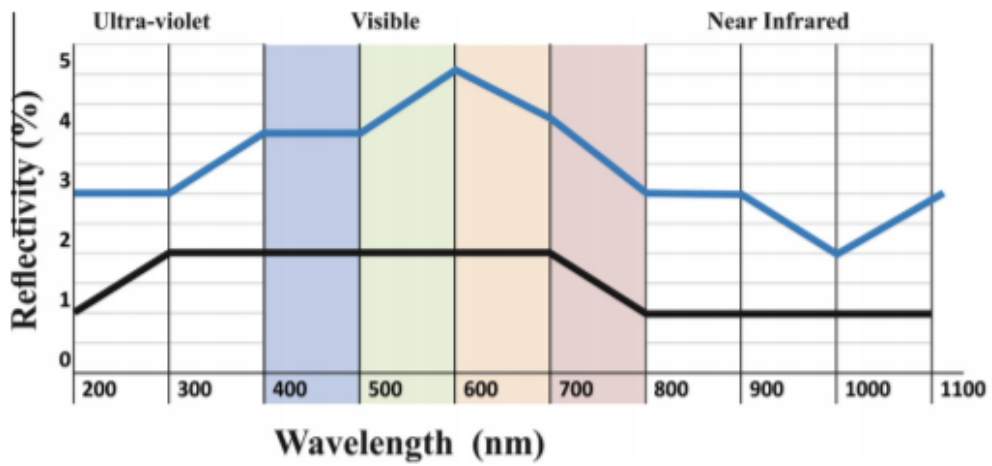The near infrared has not been used much for oil spills in the past.

Figure 1- The generalized vertical reflectance of oil and water. The blue line is the water and the black line the oil (Fingas, Brown, 2014).
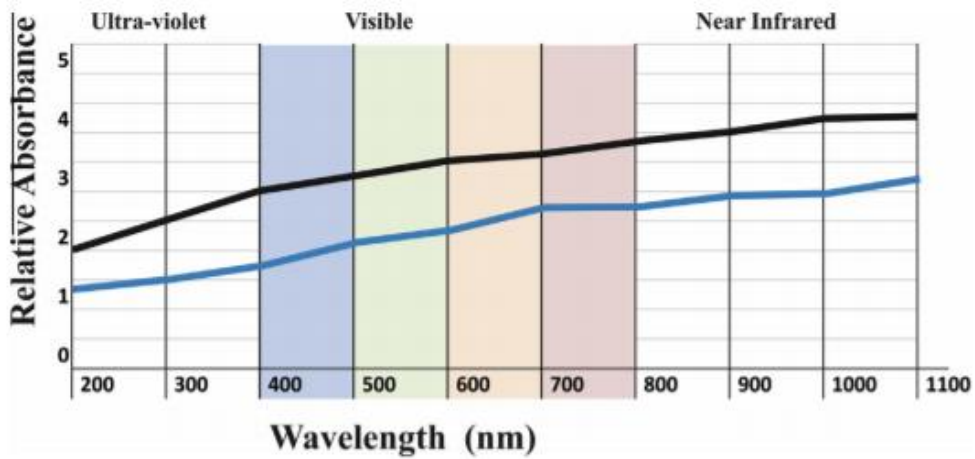

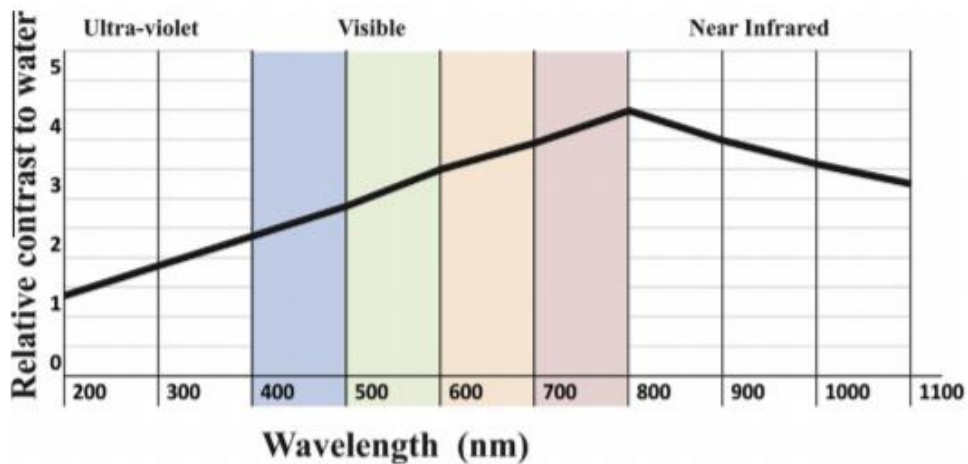Figure 2- The hypothetical absorbance of oil and water (Fingas, Brown, 2014).

Figure 3- The hypothetical contrast of oil and water represented bu the black line (Fingas, Brown, 2014).

In the infrared region, optically thick oil absorbs solar radiation and reemits a portion of this radiation as thermal energy, primarily in the 8–14 nm region. As oil has a higher infrared emissivity than water, heated oil will emit infrared radiation. In this instance, it is possible to identify the tick intermediate oil, but not the thin oil layers. Thermal infrared information regarding relative thickness is insufficient to provide information for oil spill countermeasures. Infrared oil detection is not conclusive, as several false targets, such as seaweeds, sediment, organic matter, shoreline, and oceanic fronts, can interfere (Fingas & Brown, 2014). (Brown et al., 2014).

Oil shows a high reflectance of sunlight in the ultraviolet range. Overlapping ultraviolet and infrared images have been used in the past to produce a relative thickness map of oil spills. This technique is not widely used today, as the thicknesses are not relevant for oil spill countermeasures (Chaturvedi et al., 2020).

Using optical remote sensing for the identification of oil spills presents a number of challenges. First and foremost is the requirement for clear skies in order to perform the work (Chaturvedi et al., 2020). This is a serious issue because, depending on the analyzed region and time of year, it may be extremely difficult to spot the oil. The Exxon Valdez incident exemplifies this point remarkably well. The only clear day that coincided with a satellite overpass was on April 7, 1989, despite the fact that the spill covered vast portions of the ocean for more than a month (Fingas & Brown, 2014).

Another inconvenience of satellite remote sensing is the trouble in creating calculations to feature the oil spills and the long time required to do as such. (Chaturvedi et al., 2020) However, this has changed with the availability of data and better information processing on modern satellites. New satellites like QuickBird, WorldView I, and II provide frequent ground coverage. Besides, the use of multispectral satellites has provided other tools for Earth observation (Fingas & Brown, 2014).

1.3 Fundamentals of the RADAR system and synthetic aperture RADAR

Radar is an active imaging system that operates by emitting electromagnetic energy in the microwave spectrum, operating independently of sunlight. This sensor has numerous uses in remote sensing and different study areas, such as in geology with analysis of structures and lithologies, in hydrogeology, agriculture, forest monitoring, cartography, polar regions, and oceans (Ulaby et al., 1981). The system is capable of measuring the electromagnetic field that returns to the sensor (backscatter) after its interaction with the target. The size of its wavelength is greater than the optical sensors wavelength, and its operation does not depend on many of the meteorological characteristics, as its signal is not significantly attenuated by the atmosphere,

clouds, and fog (Rebello, 2012). Radar is the only remote sensor that allows penetrability in targets, providing information from the target's electrical and geometric properties (Paradella et al., 2015).

1.3.1 Energy and electromagnetic spectrum

Electromagnetic energy has two essential characteristics for analysis in remote sensing: wavelength and frequency. The wavelength (λ) is the metric-scale distance between the wave peaks. The frequency is inversely proportional to the wavelength, is measured in hertz, this value represents the number of cycles of the wave per unit of time (*Remote Sensing Tutorials*, 2019).

The electromagnetic spectrum is a scale of electromagnetic radiation divided into: radio waves, microwaves, infrared radiation, visible radiation, ultraviolet rays, X-rays, and gamma rays. Thus, the spectrum varies from the shortest wavelengths, which carry more energy, to the longest, which carry less energy (Castilho, 2005). The radar uses microwaves, which are subdivided into several bands associated with their wavelength and frequency. The most used today are as P L S C and X bands (*Remote Sensing Tutorials*, 2019):

Banda K: de 0,75 a 2,4 cm (40 a 12,5 GHz);

Banda X: de 2,4 a 3,75 cm (12,5 a 8 GHz);

Banda C: de 3,75 a 7,5 cm (8 a 4 GHz);

Banda S: de 7,5 a 15 cm (4 a 2 GHz);

Banda L: de 15 a 30 cm (2 a 1 GHz);

Banda P: de 30 a 100 cm (1 a 0,3 GHz).

The band to be used depends on the purpose of the imaging, for example, considering a terrain with vegetation, the shorter wavelengths tend to interact with the surface layer of the vegetation, whereas the longer wavelengths can interact with the lower layers or even the soil or subsoil, as it has the ability to cross the treetops(*Teoria : Sistemas de Radar*, 2016).

1.3.2 Characteristics of the RADAR and synthetic aperture RADAR system

RADAR systems consist of a fixed side-looking antenna that emits electromagnetic energy on microwave length and captures its returned signal after it's interaction with the target, this return is called backscattering. This system requires a side view so that the return echoes of different surface targets can be distinguished (Henderson & Lewis, 1998).

The image formation is dependent upon the acquisition's geometry. There are several characteristics that can be seen that will influence the image composition. In this geometry, the slant range and ground range are the two fundamental distances to understand the image formation (Paes, 2015). (Fig. 4). In addition to these two fundamental distances, the radar geometry includes a number of angles.
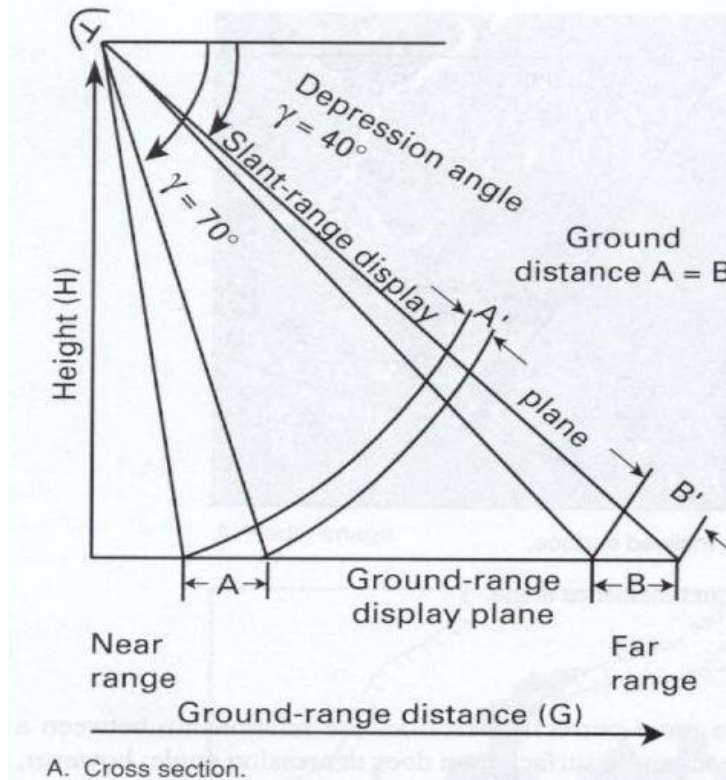
Figure 4- Basic RADAR imaging geometry system, showing the distortion in the near range (A), when stored in the slant range (A ') (modified by Sabins, 1996).

The ground projection of the beam emitted by the sensor originates two extreme incidence angles (Paes, 2015): the near range is the angle formed between the upper part of the beam (closer to the radar) and the horizontal line, and the far range is the angle between the bottom of the most distant beam and a horizontal line (Henderson & Lewis, 1998). These angles have different values due to the lateral view of the system and slope of the terrain imaged (Figure 4). The depression angle is measured between a normal horizontal line and a radar beam corresponding to the intermediate value between near and far range, whereas the incidence angle is measured between that mean radar beam and a vertical line perpendicular to the Earth's surface (Figure 4) (Henderson & Lewis, 1998).

The radar records the received data based on the slant range; consequently, the image processing system projects the image to the ground range automatically. This projection is necessary because, without it, the areas nearest to the near range would be compressed in the

image relative to the far range, as shown in Figure 4, where A and A' illustrate the distortion associated with the near range, whereas B and B' in the far range do not change because they are very close to the slant range (Sabins, 1996).

1.3.3 Spatial resolution

The ability to register and distinguish objects arranged on the Earth's surface is correlated with spatial resolution, which is crucial for defining the sensors to be used based on the intended use of the image. This parameter is defined for RADAR by the resolution in the azimuth direction (parallel to the flight path) and the resolution in the line of sight of the sensor (range resolution) (Sabins, 1996).

The range resolution is determined by the depression angle (γ) and the pulse length (τ), which is measured in microseconds, being determined by the time of the transmitted pulse. Thus, the value of the range resolution can be expressed by the following equation:

$$\mathbf{Ra = (\tau c) \cdot (2cos\gamma)^{-1}}$$

Where, Ra is the range resolution and c is the speed of light (3 x 108 m.s-1).

It can be seen that as the depression angle increases and the near range becomes closer, the resolution decreases, while the opposite occurs as the depression angle decreases and the far range becomes closer (Sabins, 1996).

The azimuth resolution is given by the angular width of the illuminated strip on the ground (λ), being directly proportional to the size of the antenna. Such a characteristic can be expressed by the following formula:

$$\mathbf{R_a = (0.7 \text{ x } S \text{ x } \lambda) \cdot D^{-1}}$$

Where Ra is the azimuth resolution, S is the slant range and D is the antenna width.

Figure 5 demonstrates that the pulse is narrower in the near range than in the far range, resulting in a higher azimuth resolution in the proximal zones as the ability to distinguish objects increases with a narrower pulse (Sabins, 1996).

DISTANCE AB = DISTANCE CD = 35m
TARGETS A & B ARE RESOLVED
TARGETS C & D ARE NOT RESOLVED
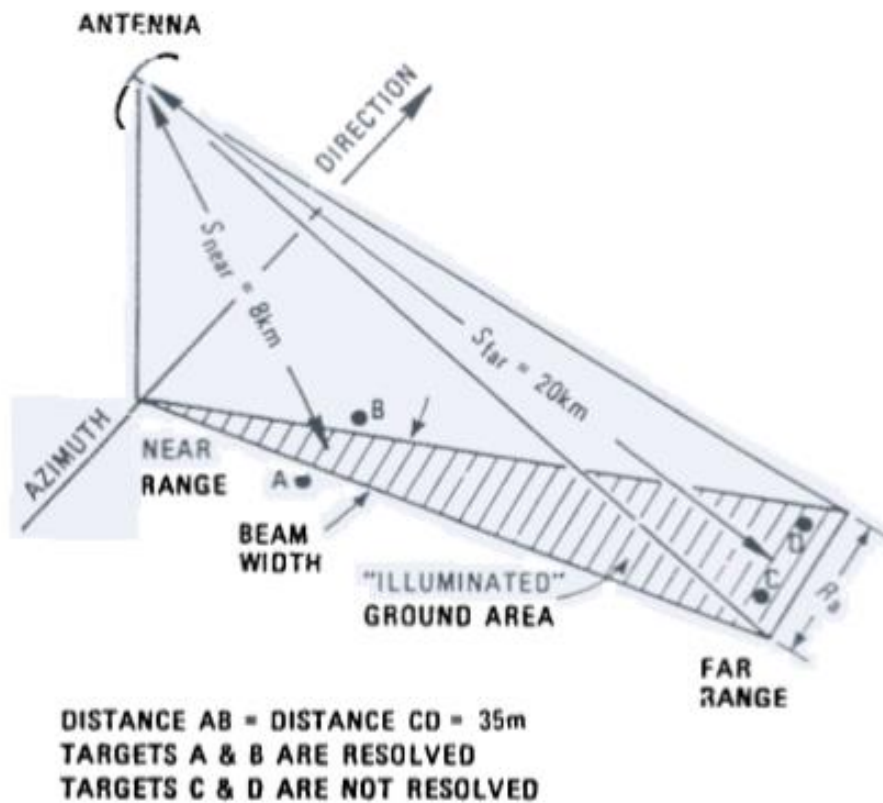
Figure 5- Azimuth resolution and beam width, AB has the same distance as CD (modified from Barr, 1969).

1.3.4 - Synthetic aperture RADAR

Side-looking RADAR systems can be either real aperture (RAR) or synthetic aperture (SAR). The main difference between these two types of systems is the method used to achieve azimuth resolution already discussed. While in RAR the size of the antenna and the distance from the ground dictates the azimuth resolution, the SAR uses a small size antenna that generates a wide beam, much larger than expected for the antenna's size, thus allowing a greater distance between the sensor and the terrain. This is only possible, because of the processing techniques applied, that are associated with the Doppler's effect principle (Sabins, 1996).

As the platform moves the SAR system sends the electromagnetic pulses during the entire time, acquiring data from the same point in several different positions (Fig.6). These radar echoes that return to the antenna are integrated, generating a composite signal, simulating a real opening. The returned signal undergoes a frequency variation due to the platform speed, this variation is the Doppler effect that directly influences the azimuth resolution (Castilho, 2005).

9
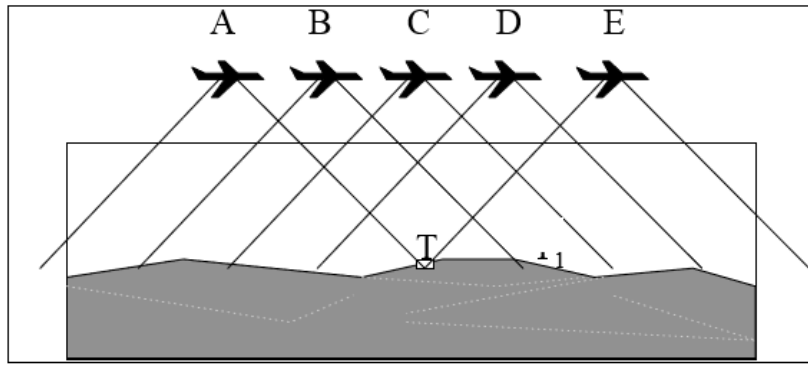
Image 6- Schematic figure of SAR data acquisition (Castilho,2005).

Due to the development of this technology, it was possible to create radars on orbital platforms, considering that the size of the antenna is no longer an essential parameter for image resolution. With a RAR it would be impracticable imaging a terrain with such a distance from the ground, since the length of the antenna would not be supported by the satellite.

1.3.5 - Electromagnetic energy interaction with the target and RADAR images's formation

The electromagnetic beam sent by the sensor interacts with the target resulting in a type of scattering depending on the wavelength used, operational characteristics of the sensor, and the geometric and textural characteristics of the target.

The reflection types can be divided into three, specular reflection, diffuse reflection, and corner reflection (Castilho,2005). The specular reflection is associated with smooth surfaces, the incident rays are reflected in the opposite direction with the same incidence angle and in the same direction (Image. 7A). The diffuse reflection is associated with rough surfaces, the rays are reflected in different directions, this happens because, although the angle remains the same as the incidence angle, the normal line changes along the surface (Fig. 7B). The corner reflection is associated with geometric surfaces and generates a strong pulse return in the same direction of arrival, this is due to the signal bouncing on objects on the surface (Fig.8).

In order to form a RADAR image, the sensor captures the backscatter of the signal sent and measures this energy, the greater this return, the greater the brightness observed in the grey levels, or digital numbers (DN) registered by the sensor (Castilho, 2005). The gray levels are a way of storing information of a scene, each image pixel is associated with a digital color value that, in this case, identifies the returned signal intensity. The number of possible digital numbers in an image is determined by the bits (binary digits) used to encode the image. Usually, the images are generated in 8 bits, meaning that the storage holds eight binary digits, which equals 256 digital levels.
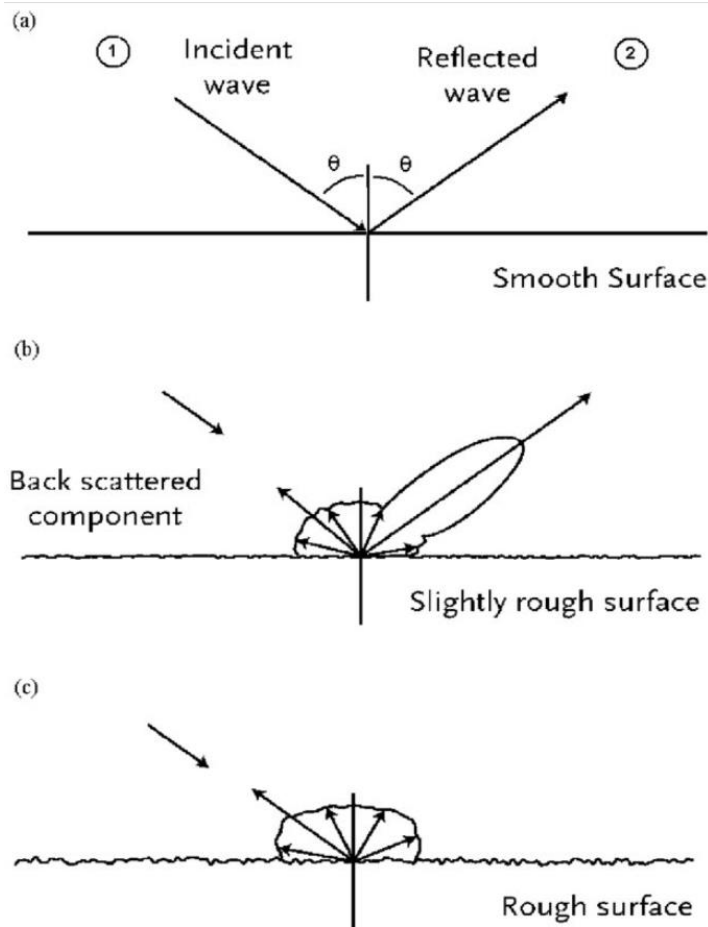
Figure 7- Different surface roughness and backscattering. A - Specular reflection. C - Diffuse reflection (Portabella, 2022).
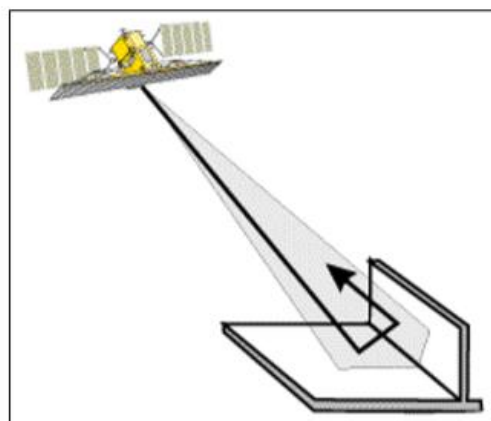
Figure 8- Corner reflection (Castilho,2005).

Analyzing the interference of the target's roughness in the image formation, a strong correlation can be noticed. In the image formation, the smoother the surface, the lower the intensity of the signal that returns to the sensor, resulting in lower values of gray levels (Sabins,

1996). A rough surface, which has diffused scattering and divides the energy at all angles will be recorded with values of intermediate gray levels (Sabins, 1996).

A corner reflection, will create backscatter pulse return in the same direction, and will present very high values of gray levels in the image.

The incidence angle (Fig.9) also has a significant effect on the image's characteristics. In theory, this angle can range from 0 to 90 degrees, but in practice, horizontal and vertical angles are avoided in favor of 25 to 30 degrees or 75 to 80 degrees (Garcia, 1982). Very little or no energy returns from a surface with specular reflection at very low incidence angles, while at very high incidence angles (80 °), a substantial amount of energy returns to the sensor (Image 9A). In contrast, to a smooth target, a surface with diffuse reflection does not present as much contrast with the changes in the incidence angle (Image 9B) (Garcia, 1982).
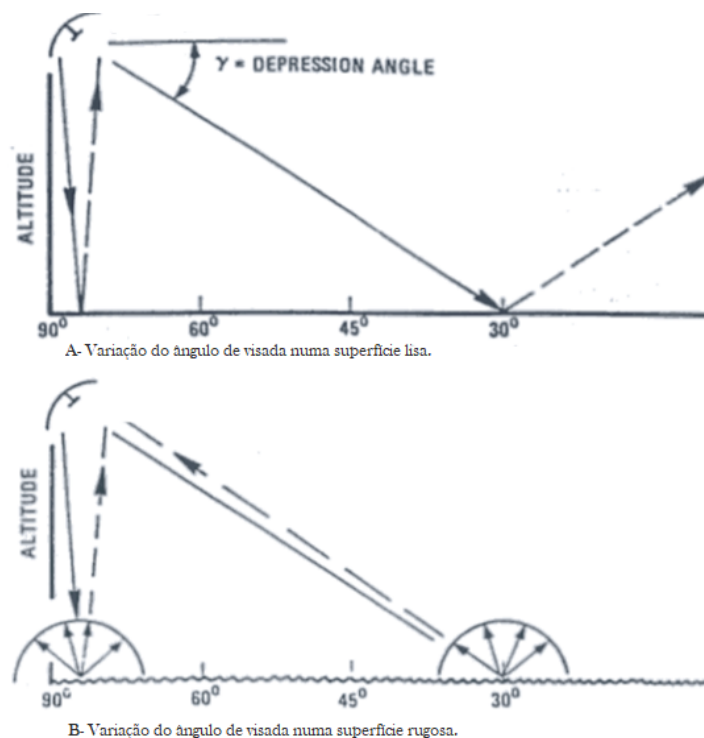
Figure 9- Incidence angles interference in the formation of the image (Garcia,1982). A-Variation of the incidence angle on a smooth surface. B- Variation of the incidence angle on a rough surface.

1.4 - Oil slicks identification through SAR

Bragg waves are the wind-generated small waves that typically characterize the ocean. These waves can be divided into capillary waves, which have a wavelength close to 2 centimeters, and short gravity waves, which have a wavelength close to 50 centimeters (Crisp, 2004).

In radar images, the ocean's backscatter is linked to surface roughness, which is in turn dependent on Bragg waves. This results in a diffuse reflection known as Bragg, which is depicted by intermediate levels of gray in the image (Image 11a) (Sabins, 1996).

The oil usually presents low digital numbers on the images. This happens because the oil attenuates the Bragg waves when it comes into contact with the ocean surface, creating a specular reflection due to the reduction in roughness (Image 11b) (Brekke & Solberg, 2005).

In images used for oil detection, it is common to find points with extremely strong backscattering in the middle of the ocean; this evidence may indicate the presence of oil platforms or ships. They produce a corner reflection with a powerful signal return (Image 10c).

Thereby, the sea displays intermediate levels of gray values in the SAR image, in contrast to the low values correlated with the presence of oil, enabling it's identification.

Considering the information presented in the preceding section, it is possible to conclude that the radar does not necessarily detect oil, but rather the smoothing of Bragg waves, which ends up creating a series of ambiguities, also known as false targets. This happens because there are other phenomena that generate such attenuation (Fingas, 2016).
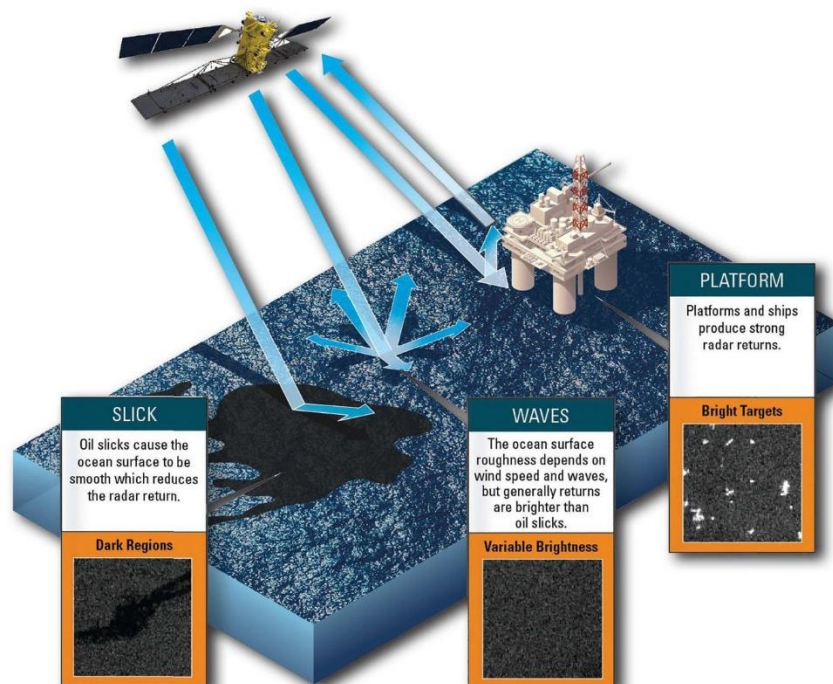
Figure 10- Sea surface scattering on (a) a rough surface without the presence of oil, (b) platform on a smooth surface with the presence of oil and (c) smooth surface with the presence of oil (Joel MacDonald, MDA Geospatial Services Inc., 2021).

The absence of wind is one of these phenomena, the Bragg waves are a result of the presence of wind on the ocean's surface. Therefore, the lack of wind results in a low contrast between sea and oil, as both will present specular reflection characteristics (Image 11a).

On the other hand, very strong winds create very big waves, that end up mixing the oil with water due to turbulence, hindering the identification (Pellon et al., 2004). Therefore, the optimal wind speed range for oil detection is between 3 and 8 meters per second (Staples & Rodrigues, 2013).

The presence of heavy rain cells also hinders the detection of oil, as it attenuates the capillary waves due to turbulence, forming an area of low backscatter in the center of the cell and high at the edges (Pellon et al., 2004) (Image12b). In addition to these, several other factors can cause such problems of interpretation, as described below (Roriz, 2006):

- Wind shadow zones, which are generated behind structures or land;
- Marine resurgence zones;
- Presence of submerged marine vegetation;
- Convergence areas generated by atmospheric convection;
- Biogenic oils, which are secreted by fish or other organisms;
- Turbulence caused by shipping.

Visual and data integration strategies are being used to address these difficulties. Silva (2009) analyzes meteorological and oceanographic graphs acquired with the closest temporal proximity achievable in his work. This method is proved to be very effective, however, requires the crossing of a multitude of data, such as: sea surface temperature, cloud top temperature, wind speed, wave height, and chlorophyll concentration. In the work of Roriz (2006) for the identification of the false targets, meteorological and oceanographic data were collected by satellites and geological and geophysical information was also used.

Keeping this in mind, it would be interesting to further investigate this simple SAR image usage. Less complexity and data would be advantageous with regard to the speed of analyses. The response velocity certainly will be less than when images with more complex information are used. One of the methodologies that have been applied and tested recently is the one present in Santos (2019) work, where transect lines cross the image and the correlation of the gray levels of each pixel is analyzed through a lagged space diagram.
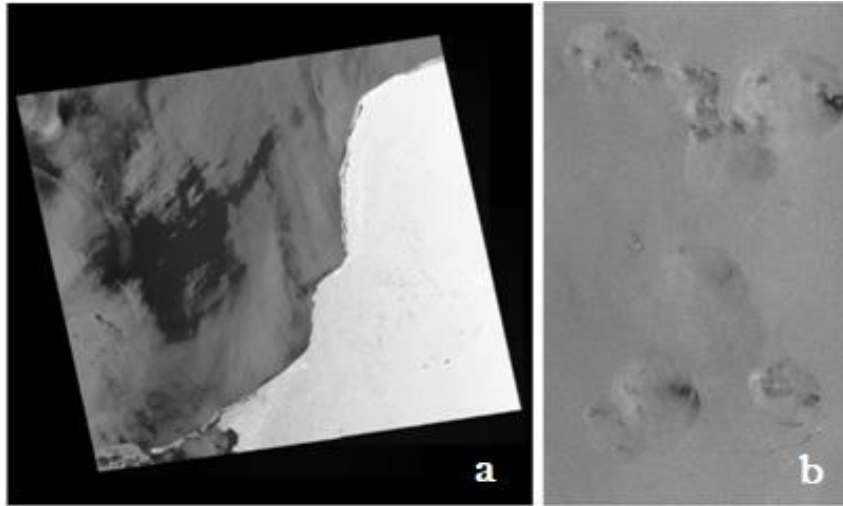
Figure 11- Images from the RADARSAT-1 satellite. (a) Areas of low signal return associated with low wind. (b) Areas of low signal return associated with presence of rain cells. (Modified by Roriz (2006)).

1.4.1 SAR polarimetry to identify the look-alike

Polarimetry is related to the orientation of the electromagnetic wave, the spreading of that wave, and phase information between the two channels, horizontal (H) and vertical (V).

An electromagnetic wave can be polarized (a monochrome sine wave with constant frequency and stable amplitude), depolarized (with random polarization) or, present an intermediate behavior between these two extremes, characterized by a certain degree of polarization (Andrade et al.,2007).

Many radars are designed to transmit polarized microwave radiation horizontally or vertically. A wave transmitted in any of these polarizations will generate a backscattered wave with a variety of polarization that can be analyzed in different ways (Andrade et al.,2007). In this case, there can be four combinations of polarizations transmitted and received.

• HH - for reception and horizontal transmission;

• VV - for reception and vertical transmission;

• HV - for horizontal transmission and vertical reception; and

• VH - for vertical transmission and horizontal reception.

Radar systems can have different polarization combinations:

• Simple polarization - HH or VV;

• Dual polarization - HH and HV, VV and VH or HH and VV;

• Quadruple polarization - HH, VV, HV, and VH; and

• Completely polarimetric - HH, VV, HV, VH, plus the relative phase between these polarizations, an important component of a polarimetric radar.

The main part of the synthetic aperture radar onboard satellites that are used for oil detection work in X-band (Coppini,2011), however, the C band has also been widely used for the same purpose. The C band Sentinel-1 has been used to monitor the sea. When talking about oil detection, VV polarization gives a better clutter to noise ratio (CNR) over HH polarization for oil slick location. Sentinel-1 is completely polarimetric and many works have been using this data for oil spot localization. The vertical polarization (VV) is desirable over cross-polarization (HV and VH) for oil identification. When analyzing data from Sentinel-1 the oil presence on the sea has almost no impact on VH or HV polarized images as for its impact on the VV energized image, thus HV (VH) polarization is less valuable for this kind of use (Chaturvedi et al., 2020).

1.5 - Sentinel-1

The following information was taken from the ESA website about their Sentinel Constellation (European Space Agency, n.d.).

The Sentinel-1 mission comprises a constellation of two satellites in polar orbit, operating day and night. This mission is the European Radar Observatory for the Copernicus joint initiative of the European Commission (EC) and the European Space Agency (ESA).

The Sentinel-1 mission includes a C band synthetic aperture radar that works in four image modes containing different resolutions (up to 5 m) and coverage (up to 400 km). It provides double polarization capability, very short overhaul times, and fast product delivery.

The mission consists of a constellation of two satellites, SENTINEL-1A and SENTINEL-1B and they share the same orbital plane, with a 180 ° orbital phase difference. With both satellites in operation, the repeat cycle is 6 days.

The Sentinel data products are made available systematically and free of charge to all data users. The data received are delivered within one hour after the real acquisition for near real-time emergency response (NRT), within three hours for priority NRT areas and within 24 hours for systematically archived data.

1.5.1- Operation modes

The sentinel one carries a C band synthetic aperture radar, working in a frequency of 5.405 GHz. It is a right-looking active phased array antenna. The C-SAR instrument supports dual-polarization operation (HH + HV, VV + VH) and single polarization (VV or HH).

SENTINEL-1 operates in four exclusive acquisition modes: Stripmap (SM);
Interferometric Wide swath (IW); Extra-Wide swath (EW); Wave mode (WV) (Fig.12).

Stripmap Mode provides coverage with a 5 m by 5 m resolution over a narrow swath width of 80 km. It is possible to choose one out of six imaging swaths changing the beam incidence angle and the elevation beamwidth.

Interferometric Wide Swath Mode (IW) combines a large swath width (250 km) with a moderate spatial resolution (5 m by 20 m). The IW mode images has three sub-swaths covering incidence angles from 29.1° - 46.0°.

This mode uses the Terrain Observation with Progressive Scans SAR (TOPSAR). This is a technique in which data is acquired in bursts, cyclically alternating the antenna beam between multiple adjacent sub-layers. TOPSAR acquisitions can provide large bandwidths and improve radiometric performance.

Extra Wide Swath Mode is intended for maritime, ice, and polar zone operational services with wide coverage and short revisit times. This mode also uses a TOPSAR technique using five sub-swaths, resulting in a lower resolution (20 m by 40 m).
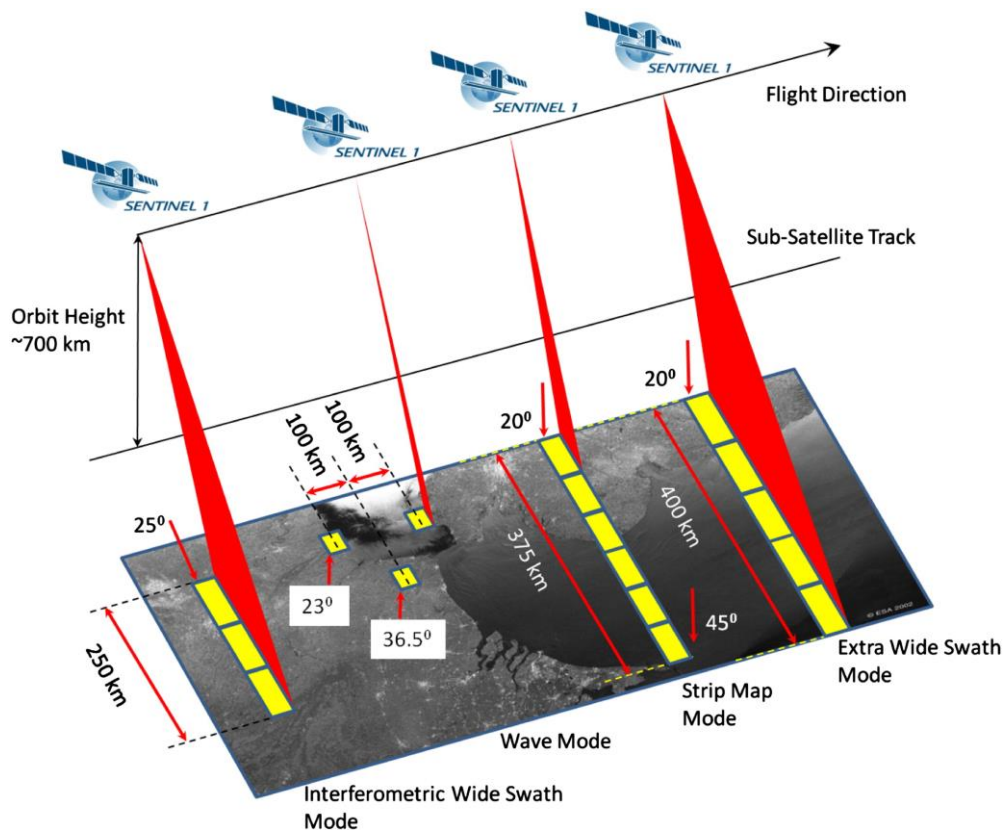
Figure 12- All the function modes of Sentinel- 1 (European Space Agency-b, n.d.).

The Wave Mode can help determine the direction, wavelength, and heights of waves on the open oceans. This mode is composed of stripmap images of 20 km by 20 km, acquired alternately on two different incidence angles. Wave images are acquired every 100 km, with images on the same incidence angle separated by 200 km.

As pointed before an important factor to consider when interpreting SAR images is that the contrast between oil infiltrations and their surroundings depends largely on the angle of incidence of the radar beam. Incidence angles of 10° - 40° improve the detection (Pellon et al., 2004) as discussed in the section 1.3.5.

1.5.2- Processing Levels

Three possible processing levels can be downloaded from the Copernicus website.

Level 0 – The products are compressed and unfocused SAR raw data.

Level 1- The raw data goes through several processing steps. Two product types can be chosen for further analysis:

• Single Look Complex (SLC) products are provided in slant-range geometry. The SAR data has been georeferenced using satellite's orbit and attitude information

• Ground Range Detected (GRD) products consist of focused SAR data, which has been detected, multilooked and projected to ground range using an Earth ellipsoid.

Level 2- This level is especially dedicated to maritime applications. Geophysical information is derived from SAR data providing the following information layers (Lehner & Tings, 2015):

• Ocean Wind field (OWI)

• Ocean Swell spectra (OSW)

• Surface Radial Velocity (RVL)

1.6- Space-Series

Space-series is another essential term used to comprehend the methods employed in this work.

Based on the paper by Unwin and Hepple (1974), the following paragraphs aim to explain the fundamental theory of spatial series.

A space series is a collection of observations on a variable (w) organized with considering to two spatial coordinates (u, v) that are typically interdependent. Often the coordinates u and v are represented as the ordinates and abscissa of a Cartesian system.

Spatial series can be divided in the following ways:

Between continuous and discontinuous data- Continuous data manifests itself over the entire surface, such as height above sea level. Discontinuous data are represented punctually, using population data for each city as an example.

Between data located in a regular matrix, such as, in this case, a Cartesian matrix, and in an irregular matrix associated, for example, with country borders.

This data distribution may reveal a certain structure, pattern or spatial form, and it is likely that a point (Ut, Vt) or a region in a matrix is related to the values of other points or regions.

The lack of statistical autonomy of the points in the series is called spatial dependence. Thus, the spatial series are not independent random variables, but rather present a certain correlation in which the values in a region provide statistical information about the probable value of the adjacent areas.

2 - Materials and methods

In this chapter will be presented the materials and methods used.

The method consists of the use of transect lines and space lagged diagrams to try differentiating various targes on the ocean surface.

The materials are the chosen Sentinel-1 images and the results of a previous research that made use the same methodology to images from RADARSAT-1.

2.1- Method

Transect lines cross the radar image and provide the grayscale value (DN – Digital Numbers) of each pixel they pass through. These values are proportional to the signal amplitude that is returned to the antenna as a result of electromagnetic energy pulse interaction with the targets (Silva, 2013).

To put it another way, the transect line is nothing more than a collection of quantitative measurements distributed in space at a specific point in time, representing the state of the system at that time. This space-distributed sequence of values (DN(X)) generates a one-dimensional spatial series and may exhibit some degree of dependence between values.

As stated previously, a spatial series is a collection of observations on a variable (w) ordered in relation to two spatial coordinates (u, v) that are generally interdependent. The lack of statistical autonomy among series values is known as spatial dependence. As a result, the spatial series are not random variables, but rather exhibit a certain correlation in which the value in one region provides statistical information about the likely value of the adjacent areas.

The transects are analyzed by making "state-spaces," which means that the values are plotted in a mathematical space with orthogonal axes. These axes are the same as the DN values, so each marked point represents a pixel and its value, which describes the state at that moment. The DN(X) values are plotted on the graph in the order of the transect line, which has a clear beginning and end. This means that the points will describe a trajectory, which will define a state space that represents the transect line.

Within this space, the trajectories derived from the spatial series have a propensity to occupy certain regions while avoiding others, thereby generating a signature that can be characteristic of the object under investigation.

Based on the research of Packard et al. (1980), Silva et al. (2019) developed a method used in this work employing the idea of "state spaces." Such states, however, are spatially lagged, i.e., a transect line will be plotted on the graph and these same values will be lagged in space, defining the pair (ND(x), ND(x+k)), where k is an integer number of pixels. Thus, for k=1, the pixel DN(X) will be plotted on the X-axis, and the value of the pixel immediately ahead defined on the transect line will be plotted on the Y-axis, while for K=2, the Y-axis will represent two pixels after DN(x), and so on. As a result of the concept presented, a correlation diagonal can be defined, which represents the maximum condition of dependence of the values where ND(x) = ND(x+k).

This methodology shows the correlation between the pixels of the spatial series in a geometric way, producing a space of correlations that records the signatures associated with the target, resulting in visual constraints and preferred spatial directions of arrangement.

2.2- Materials

For this project, three images were downloaded from the Copernicus Open Access Hub website (*Open Access Hub*, n.d.).

The employed mode is IW, which is considered the default mode of operation for Sentinel-1 in the littoral zone (Vachon & Wolfe, 2008).

As previously indicated, GRD mode level 1 is the most effective processing method for this application. The image bands analyzed are the one related to the amplitude with VV polarimetry, since the HH polarimetry present no contrast between the backscatter of oil and sea.

Using the SNAP software, a subset of each image was generated, and the FROST speckle filter was applied.

Several transects were drawn and exported using SNAP, than MATLAB was used to generate lagged state space diagrams.

The selected images and their respective transects are displayed below.

The first image to be analyzed is the one on the Atlantic sea (Fig.13), 50 km from the Bahia coast. This oil is very well known and has 192.8 km2 (Ascom Ufal, 2019).

The second image is from the black sea (Fig.14). A big leak occurred on 07/08/2021 at the oil terminal at Yuzhnaya Ozereyevka near the port of Novorossiysk.

The Russian Academy of Science's (RAN) space research institute claimed a satellite photograph obtained on Sunday revealed the scale of the oil spill to be over 80 square kilometers (BBC News Русская служба, 2021).

The third image is from the Persian Gulf (Fig.15). An oil field is located on Ak Khiran where the oil spill was reported on 10th august 2017, 130000 liters licked on the sea. (European Space Agency-c, n.d.)

In the figures 13, 14, 15 and 16 we can see the subsect of the chosen images and it`s respective transect lines. The lines were placed in the horizontal and vertical positions in order to notice if there is any difference between the interactions horizontally and vertically, since the image is a polarized image.
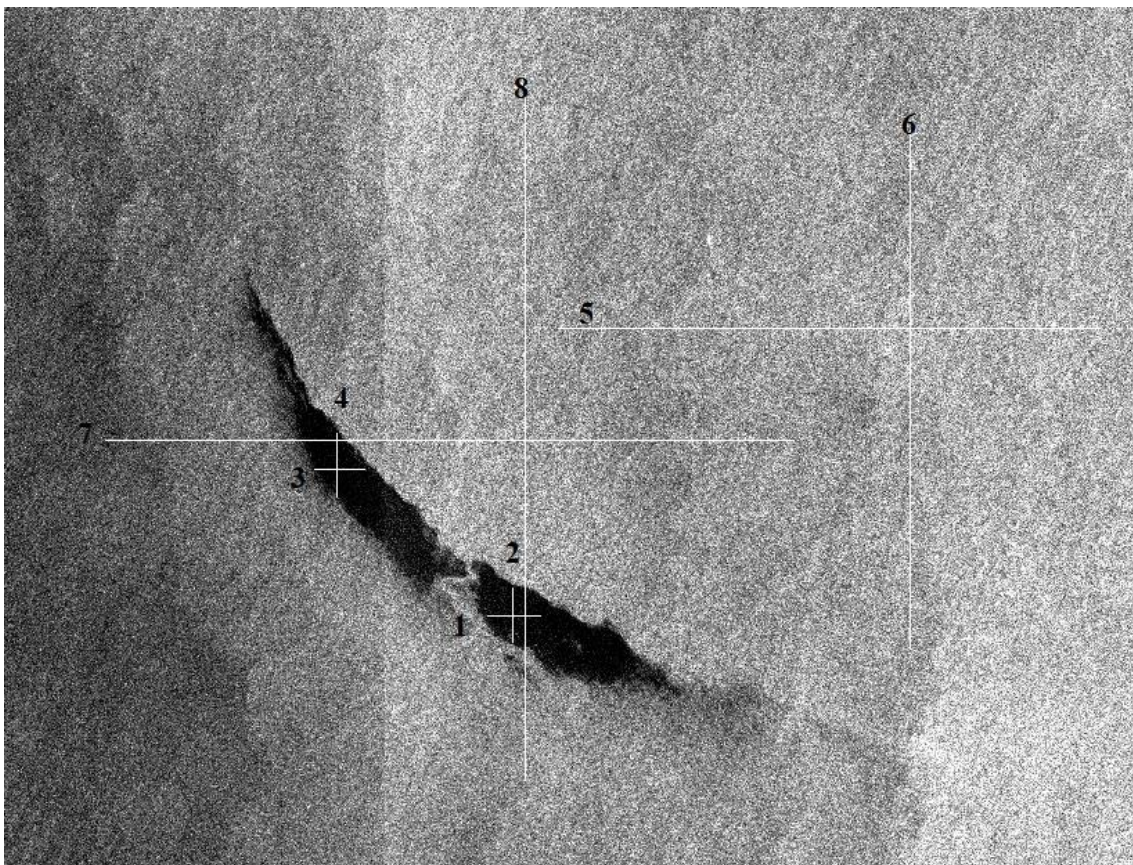
Figure 13- Oil spill on the Atlantic sea - Sentinel1A band C satellite image shows oil slick 50 km off the coast of Bahia on 28 October, 2019. Transect lines and it's numbers can be seen in the image (*Open Access Hub*, n.d.).
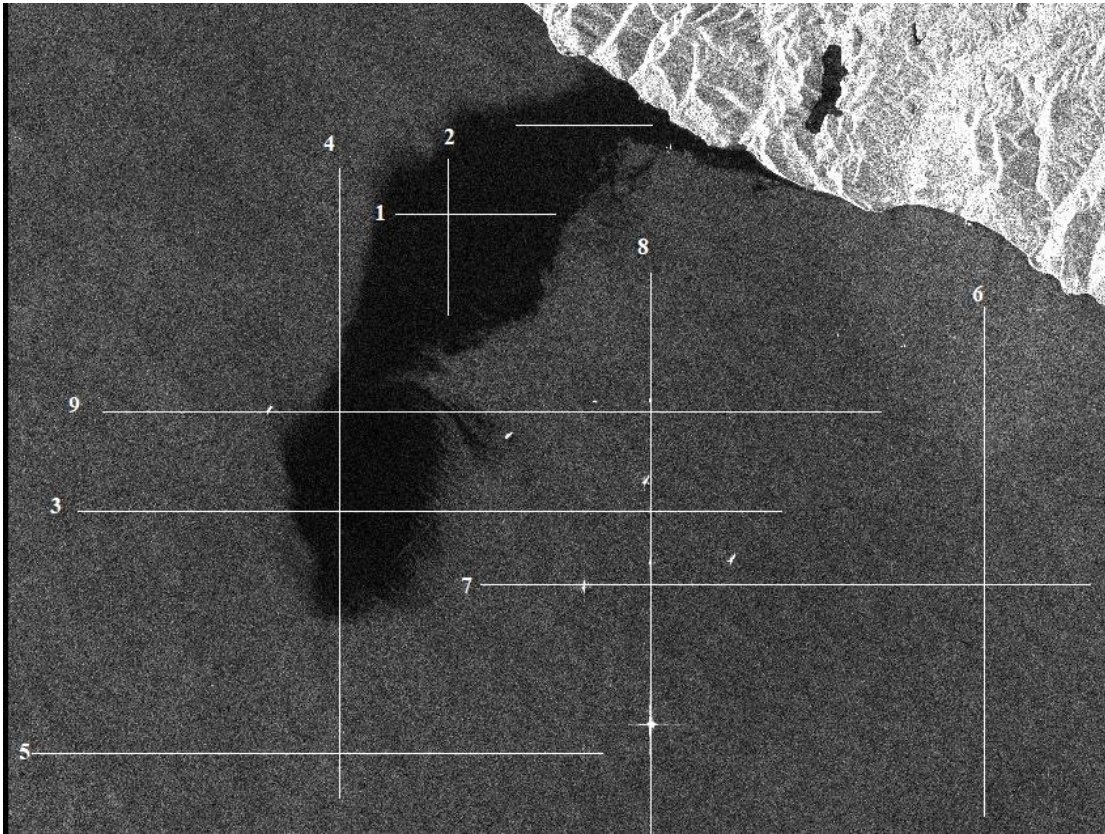
Figure 14- Oil spill on the Black sea – Using Sentinel1A band C IW GRD satellite image 80 square km near the port of Novorossiysk on 8th August 2021. Transect lines and it's numbers can be seen in the image (*Open Access Hub*, n.d.).
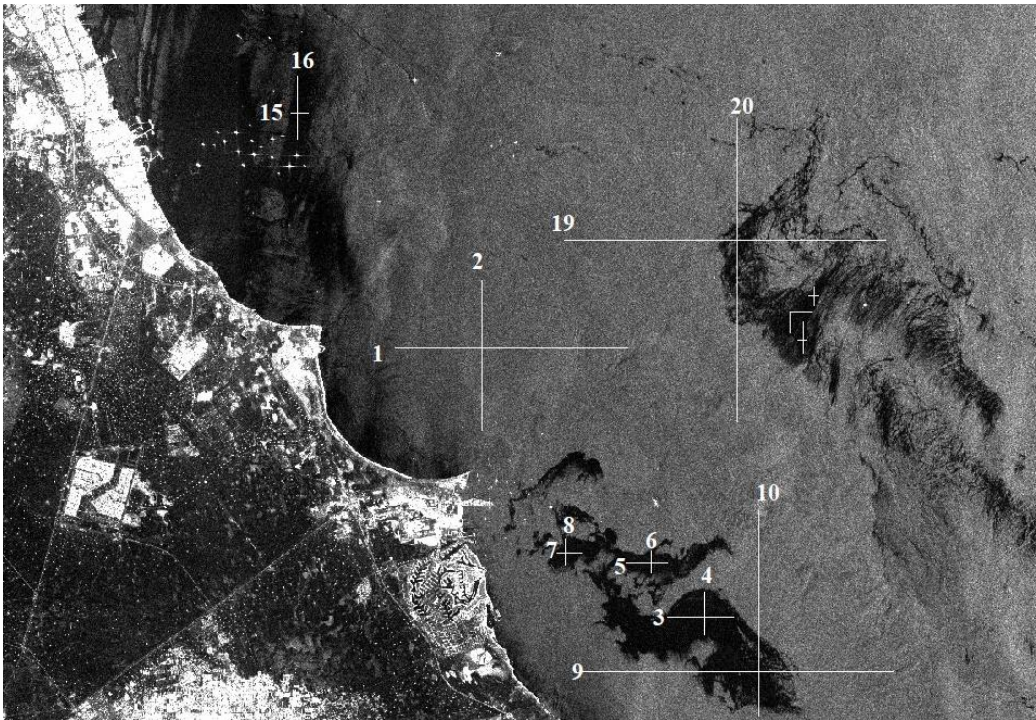
Figure 15- Oil spill and false Alarm on the Persian Gulf using Sentinel 1 band C IW GRD mode, close to Al Khiran on 10th August, 2017. Transect lines and it's numbers can be seen in the image (*Open Access Hub*, n.d.)
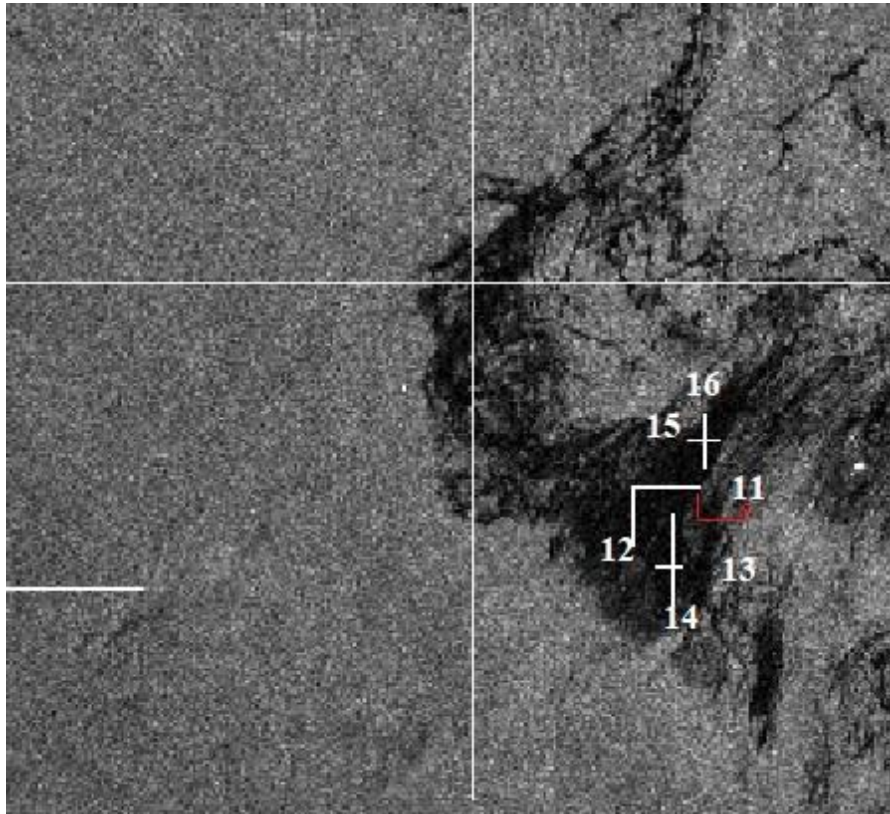
Figure 16- Subsect of the Persian Gulf image , located close to Al Khiran on 10th August, 2017. Transect lines crossing the false alarm (*Open Access Hub*, n.d.).

2.3- Previous work performed

In previous work (Silva, 2019), a RADARSAT-1 image acquired in ascending ScanSAR Narrow-1 mode was utilized. The image was acquired at 00:11:10 GMT on July 22, 2001, which corresponds to July 21, 2001 at 19:11:10 local time. This Satellite works in the X band and the Narrow1 mode has an acquisition angle varying from 20 to 39 degrees.

Figure 17a depicts a region of the ocean devoid of targets, while Figure 17b depicts a region of the ocean containing targets of interest. On these images, ten horizontal and ten verticals transect lines passing through the following targets were drawn and analyzed:

Sea: H1, H2 and H3;

Sea crossing oil spots: H4;

Oil: H5, H6 and H7;

False target: H8, H9 and H10 (Fig. 17).
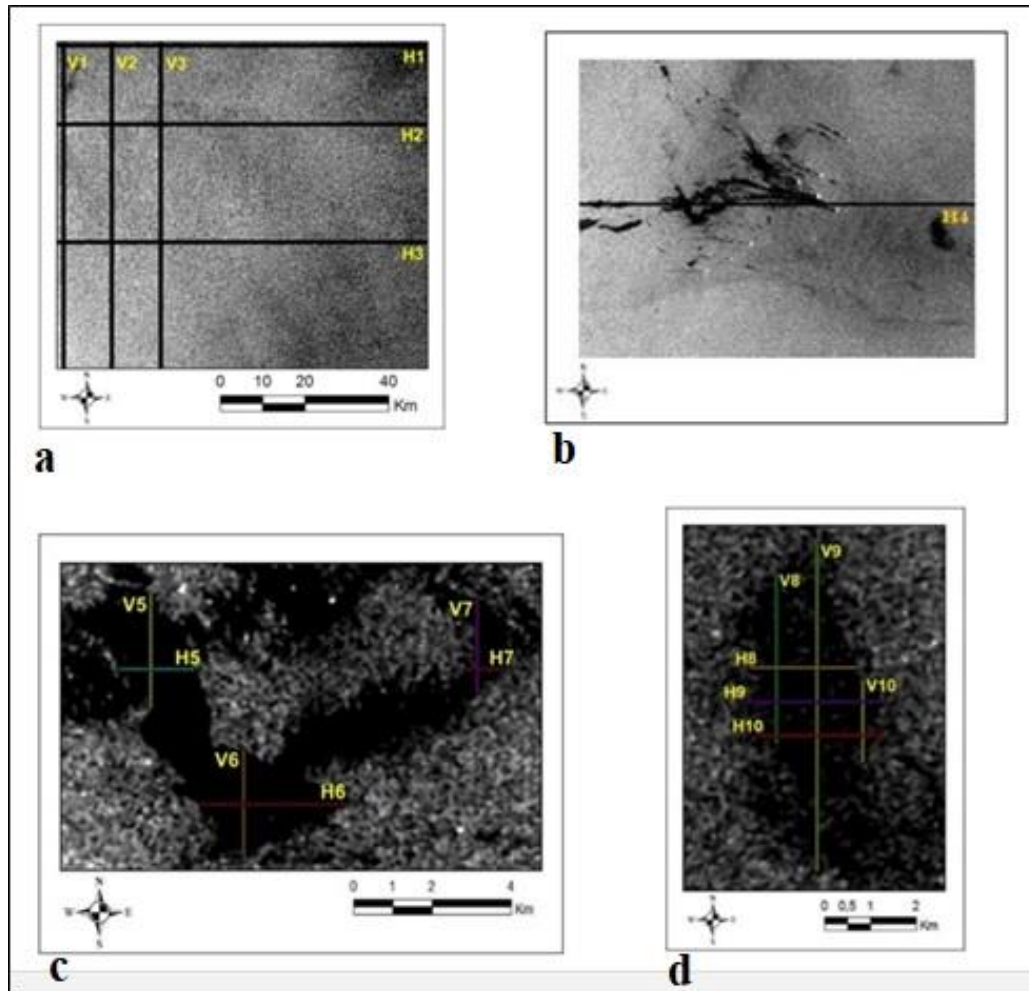
Figure17: Transects through the RADARSAT-1 image of oil spills and false alarms- Gulf of Mexico.

In this study, it was determined that the suggested technique is promising; however, tests in various locations and under various conditions are still lacking (Silva,2019).

The diagrams (Fig.18 and 19) are representative of each type of target, the ocean has a very distinctive and stable trajectory, and different signatures were generated for the oil target and the false target, allowing for their differentiation:

- Ocean: The trajectory depicted in the diagrams evolves into a collection of points.
- Oil: Points migrate to abscissa.
- False alarm: A preferred square area of point occupation is defined.
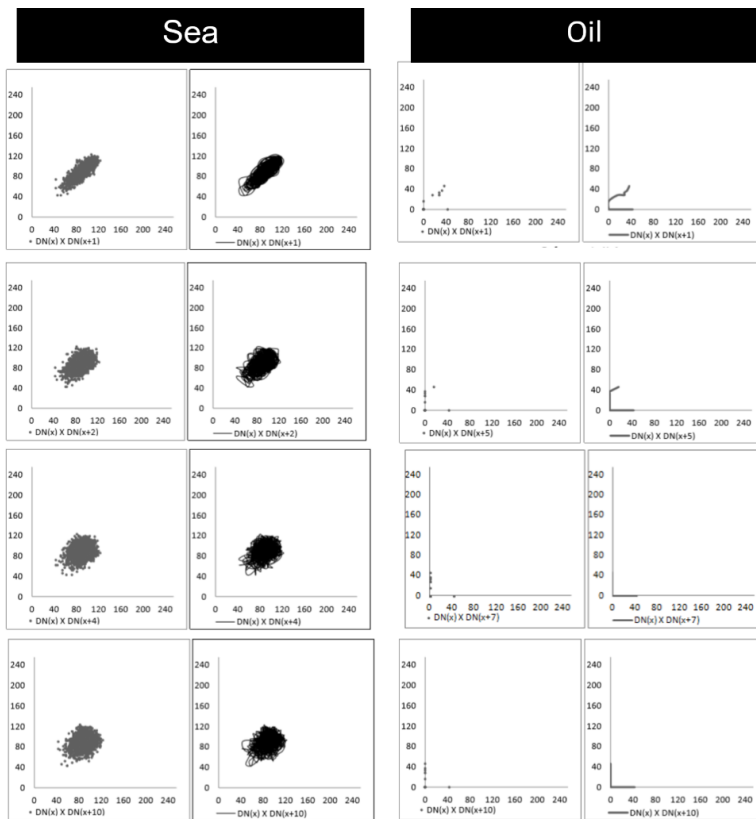
Figure 18- Signature for oil and sea analyzing a RADARSAT-1 image.
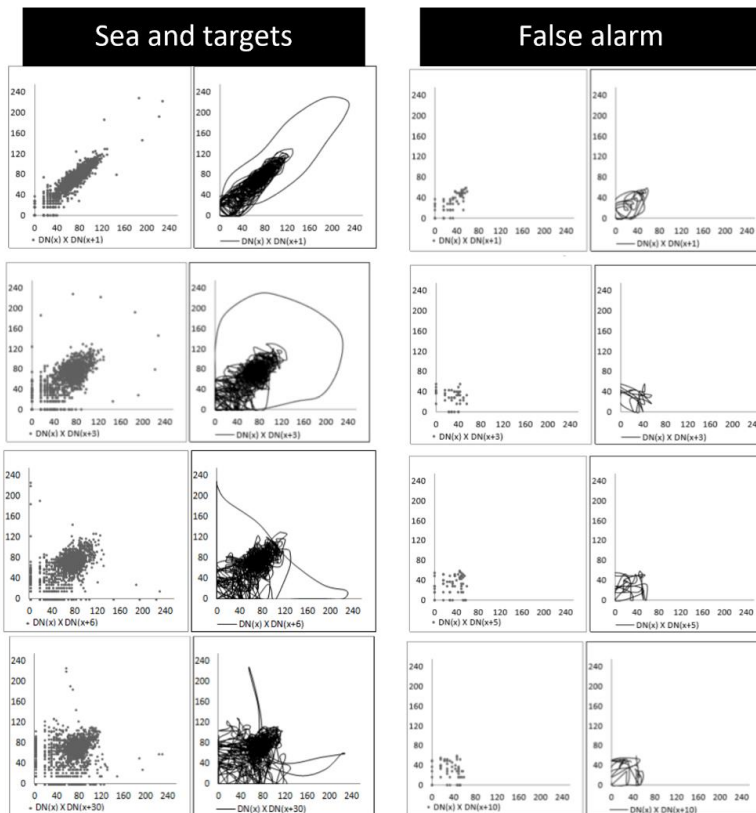
Figure 19- Signature for "sea, vessels and oil" and false alarm analyzing a RADARSAT-1 image.

On the basis of this work, it is possible to draw the inference that the trajectories that are produced by the lagged state diagram are diagnostic of various categories of targets.

The results that were obtained from this previous work will be contrasted with the findings of the spaced lagged diagrams obtained from Sentinel-1.

3- Results and discussion

The main results will be presented in the following pages, one transect line of each target for each image was chosen to be shown in this report, the profile plot of the transect will be presented and the main diagrams.

3.1- Results

3.1.1- Atlantic Sea

Transect lines crossing the Sea (Fig.20-25):

The width of these transect lines exceeds 4500 pixels. The Bragg-type reflection explains why their gray level values are predominantly between 45 and 90 (Figure 23). In the representations of the lagged state diagrams, the first DN(x) X DN(x+1) graph displays a trend that is near to the correlation diagonal (Figure 24), and this trend may be observed faintly until the DN(x) X DN(x+3) diagram.

The geometric representation stabilizes in the DN(x) X DN(x+4) diagram, and the points tend to cluster around the coordinates (65,70).
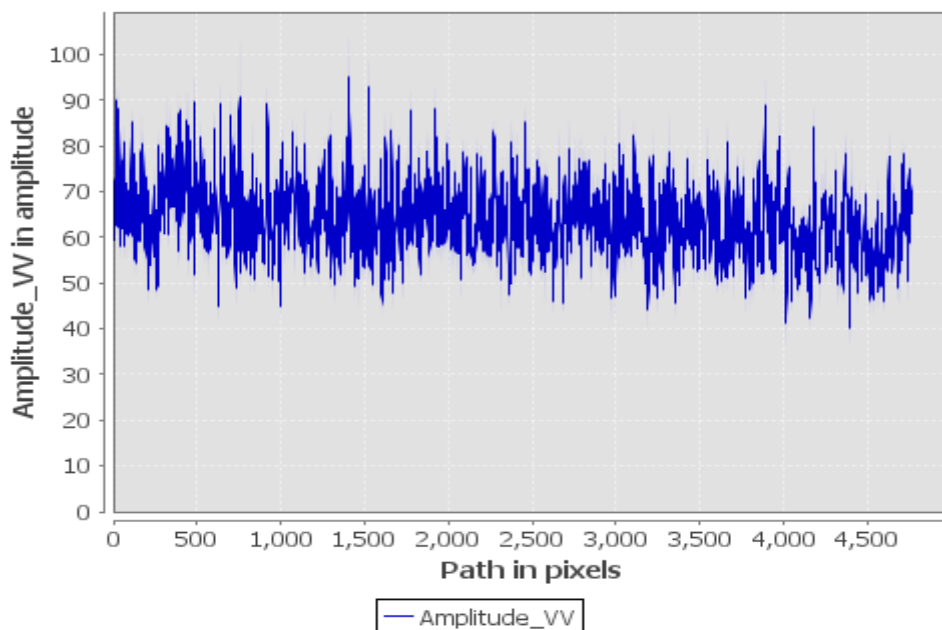
Figure 20- Values of DN (x) along transect line 5 in the Atlantic Sea.
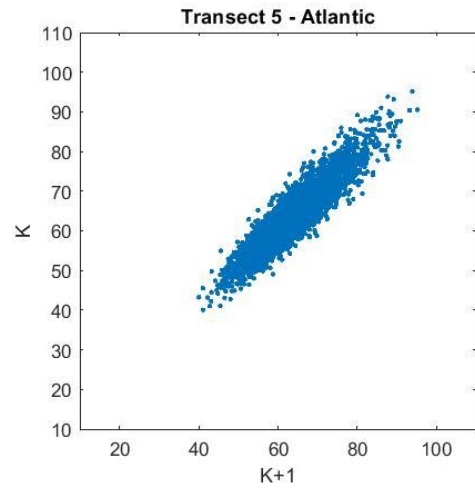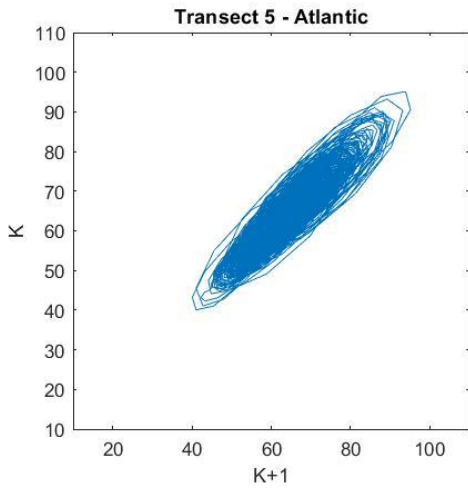
Figure 21- Lagged state space diagram DN(x) X DN(x+1)
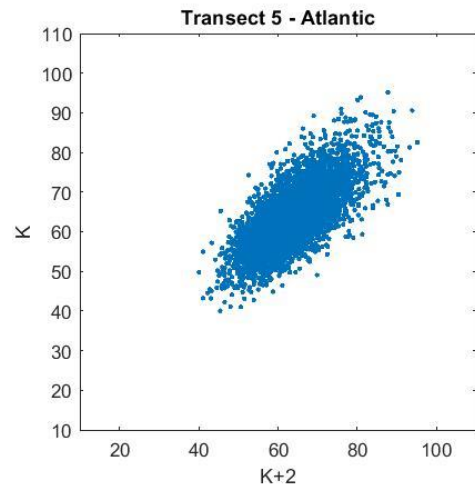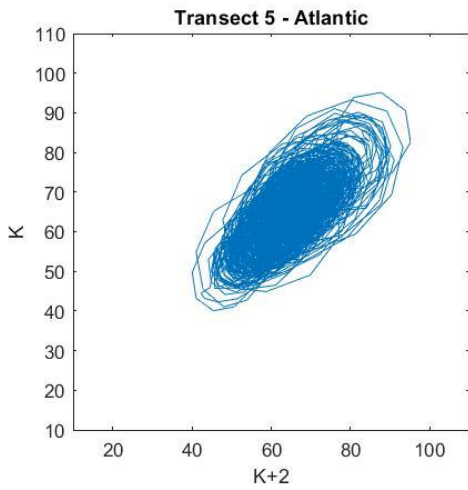
Figure 22- Lagged state space diagram DN(x) X DN(x+2)
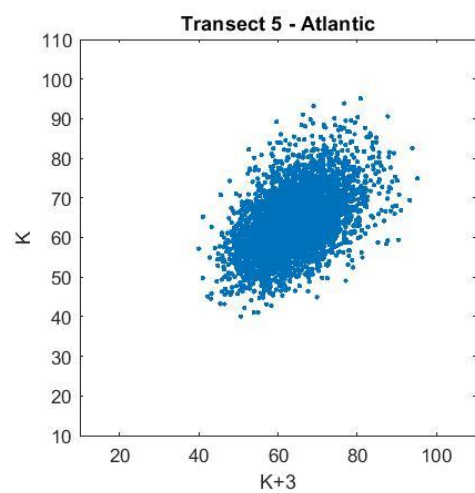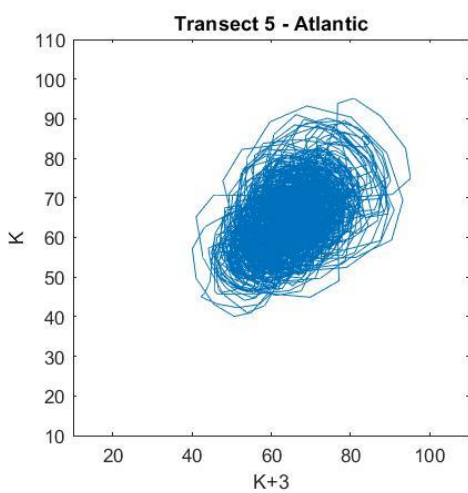
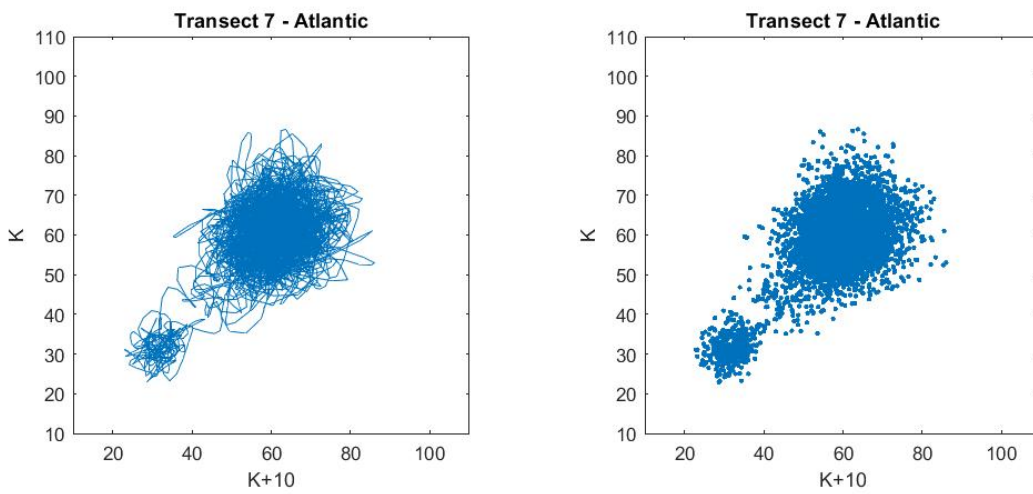Figure 23- Lagged state space diagram DN(x) X DN(x+3)
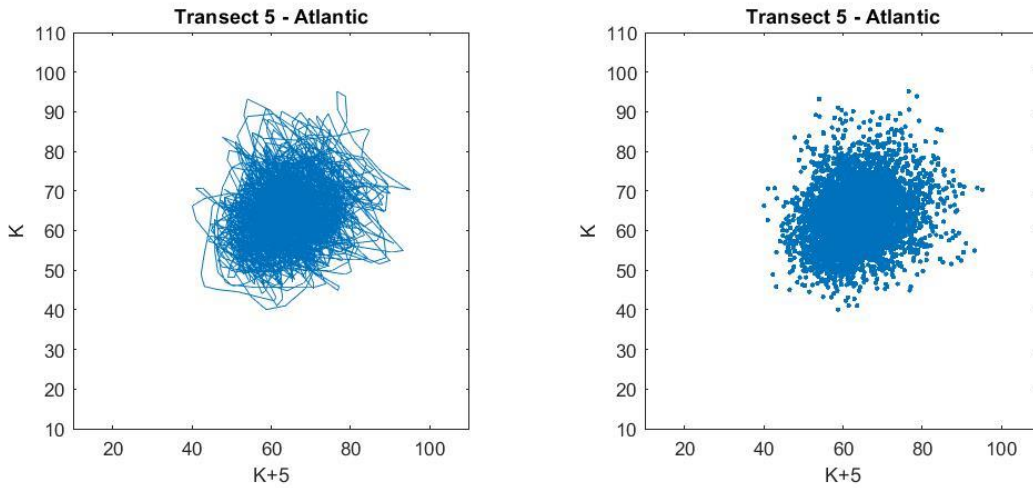
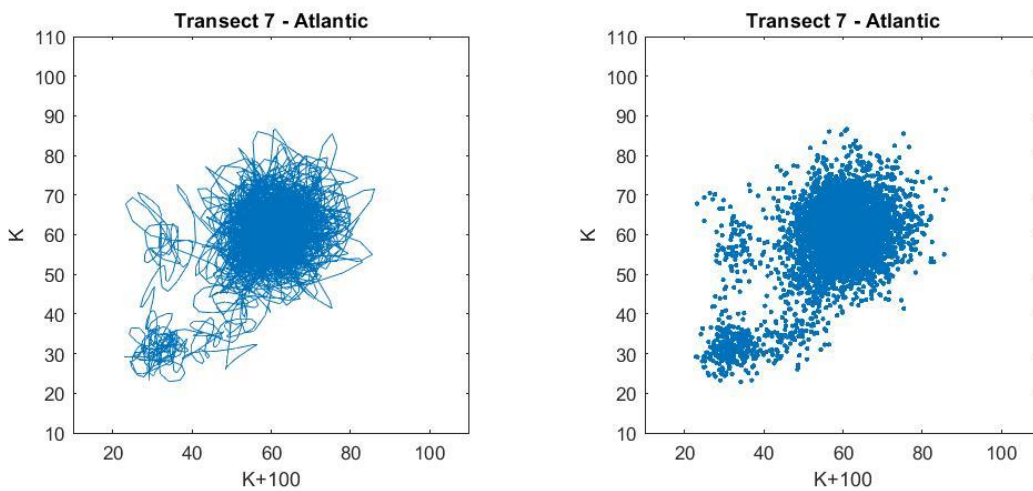Figure 24- Lagged state space diagram DN(x) X DN(x+5)

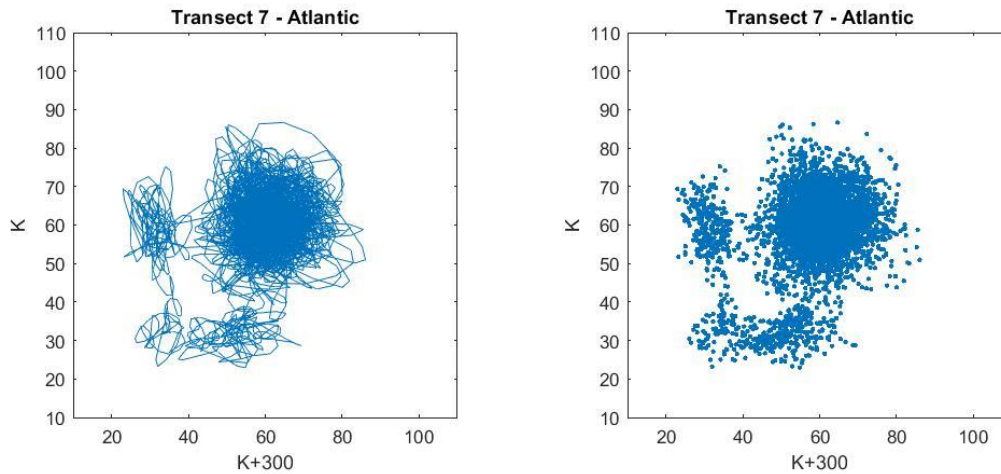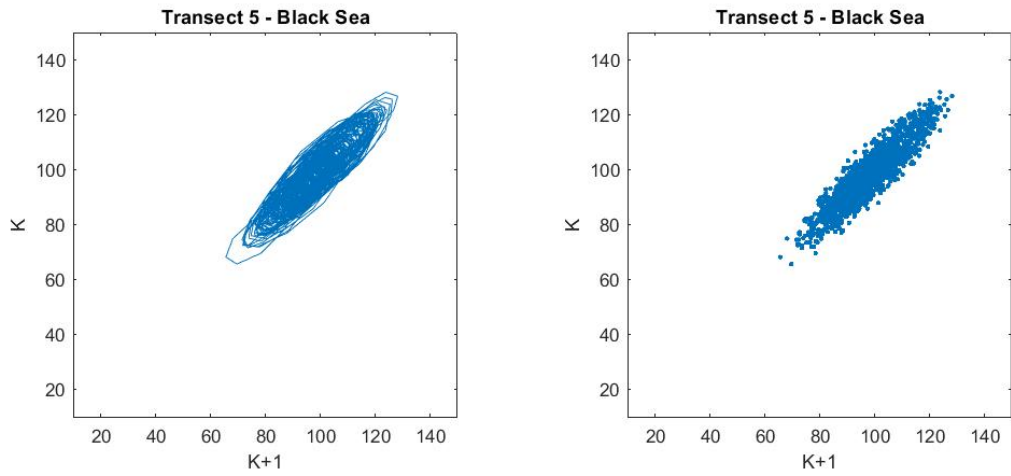Transect lines crossing oil (Fig. 25-28):

The width of the transect lines on the oil slicks ranges between 475 and 575 pixels. Due to the increased amount of specular reflection, their gray level values are lower than those of the ocean. As in the ocean, the tendency of the points in lagged state diagrams is to migrate from the main diagonal to a cluster of points with the center at (35,35) (Fig. 28). However, from the K+4 diagram onward the signature stabilizes.
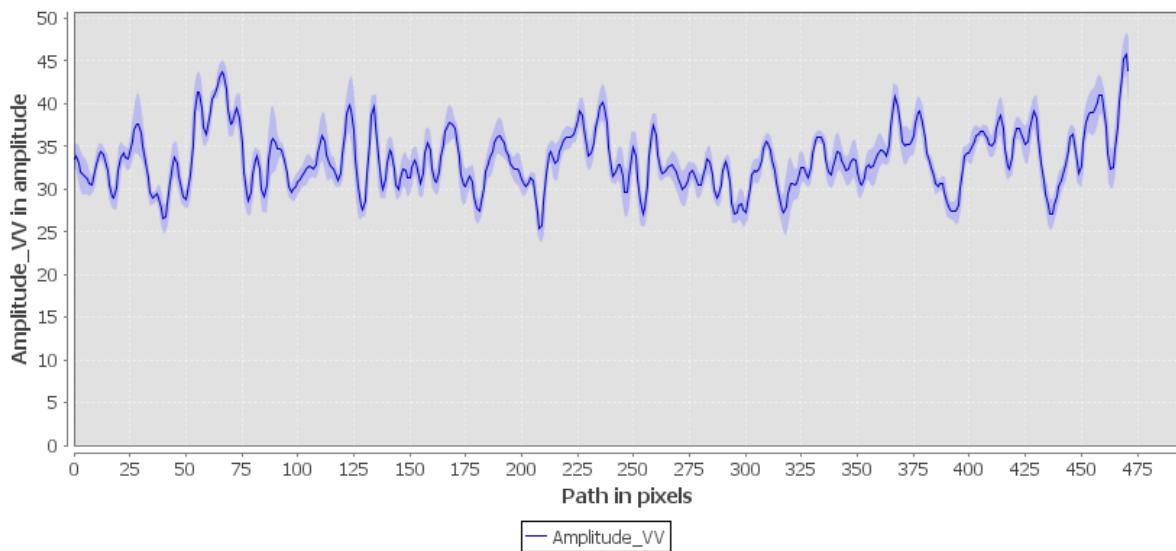
Figure 25- Values of DN (x) along transect line 1 in the Atlantic Sea.
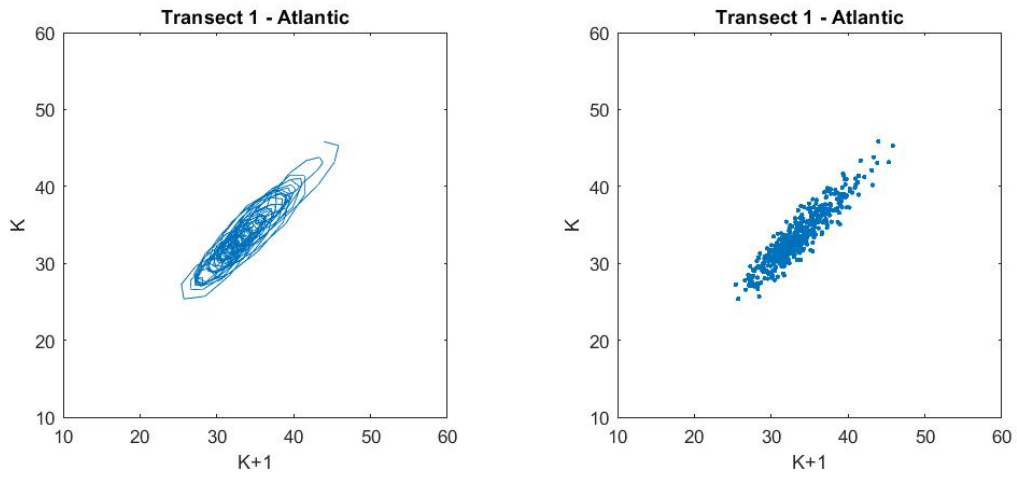
Figure 26- Lagged state space diagram DN(x) X DN(x+1)
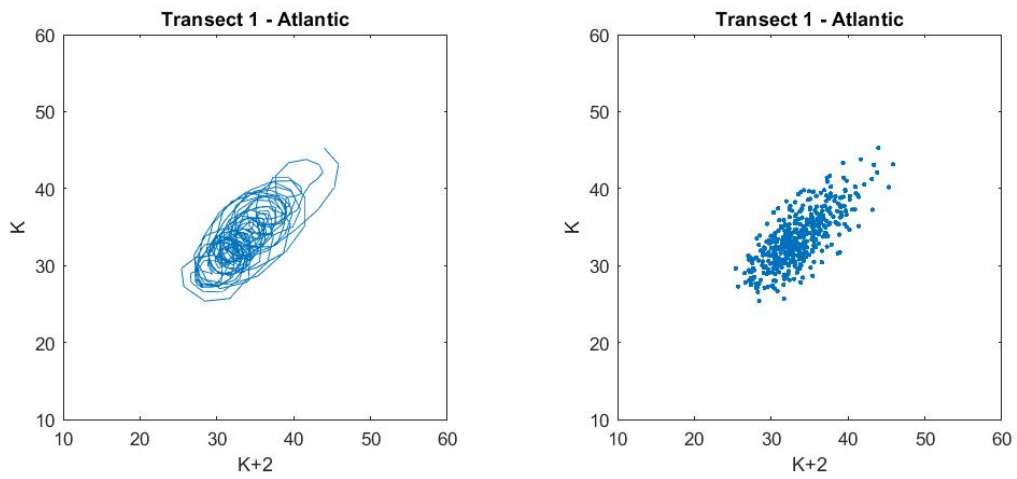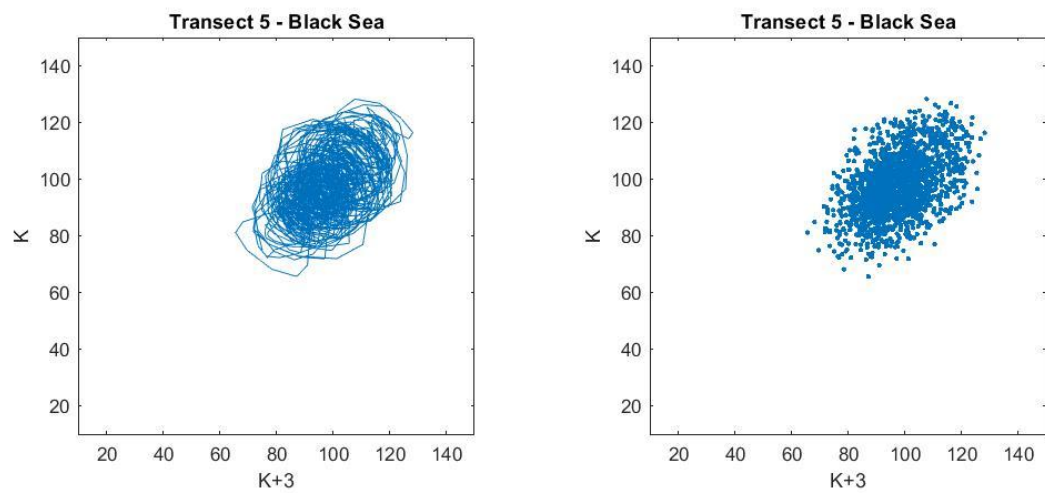

Figure 27- Lagged state space diagram DN(x) X DN(x+2)
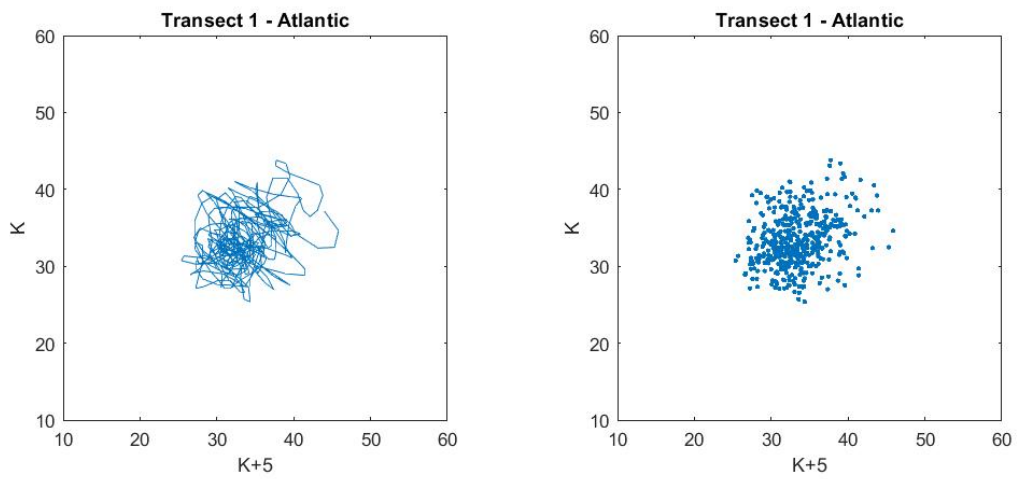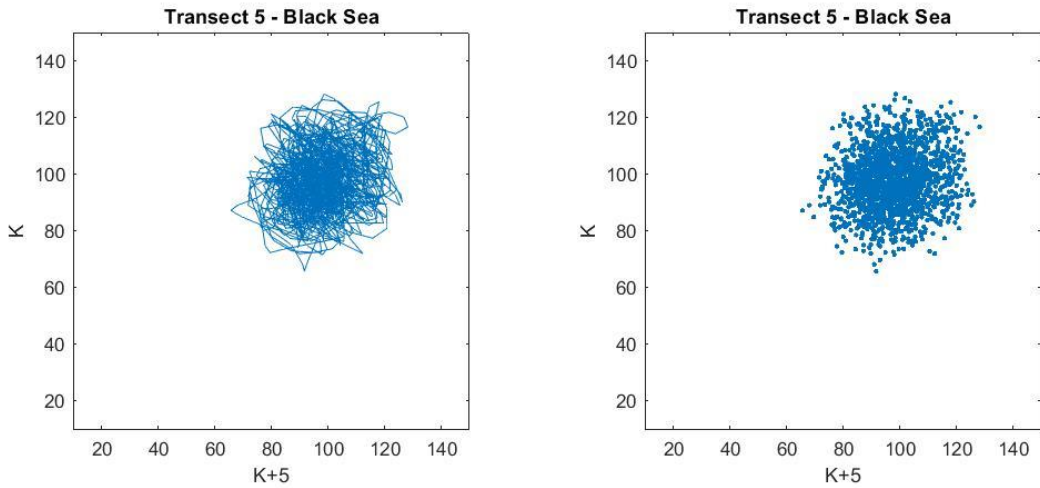

Figure 28- Lagged state space diagram DN(x) X DN(x+3)

Transect lines crossing the Sea and oil (Fig. 29-34):

These Transect lines consist of more than 6000 pixels and traverse both water and oil (Fig. 29). Due to the diversity of targets, their DN values vary widely, with intermediate levels connected with Bragg scatting and low values related to the oil specular return. There are two clusters connected to the correlation diagonal for the lag DN(x+1). For the delays from DN(x+4), there are two clusters with centers in the coordinates (30,30) and (60,60), exhibiting a poor connection to the correlation diagonal (Fig. 31). A third cluster with coordinates (30,60) can be distinguished with the passage of time lags (Fig.33).

As seen in the k+300 plot, there was a posterior migration of the points in the lower portion of the plot with values between (30, 40-60) (Fig. 34).
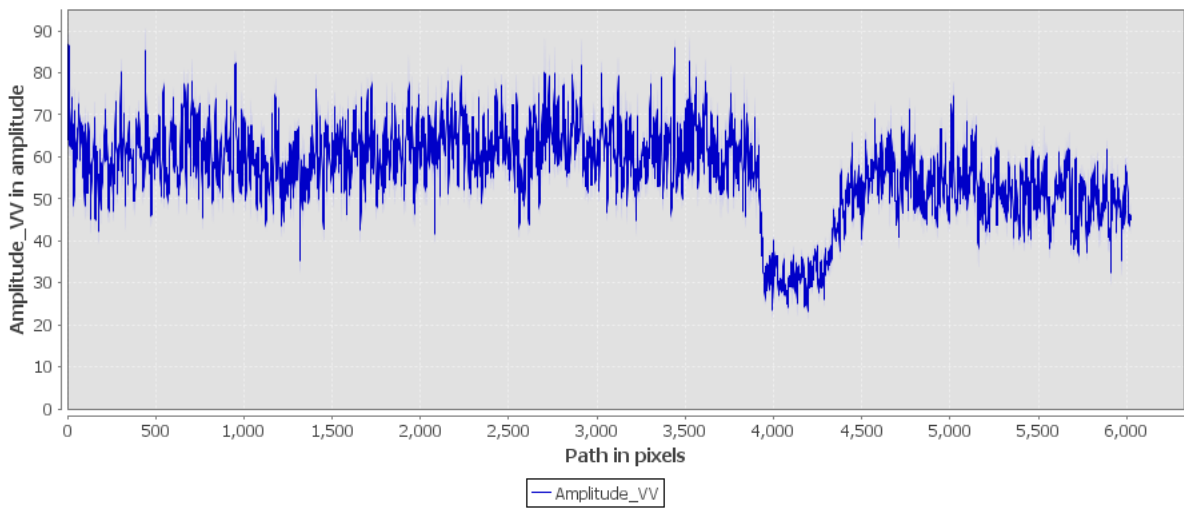
Figure 29- Values of DN (x) along transect line 7 in the Atlantic Sea.
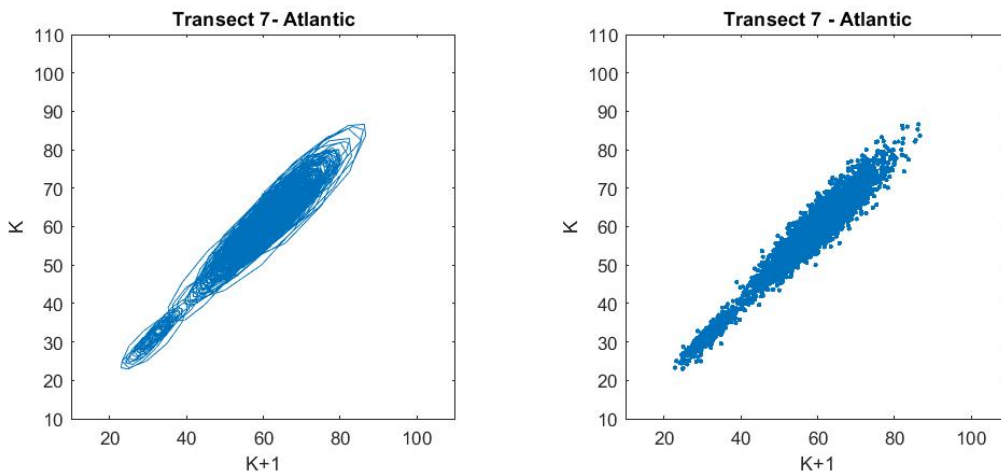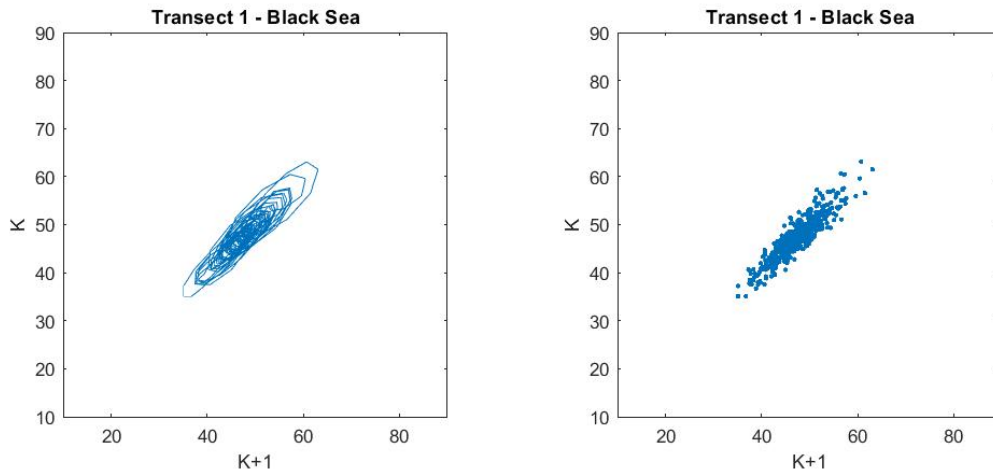

Figure 30- Lagged state space diagram DN(x) X DN(x+1)
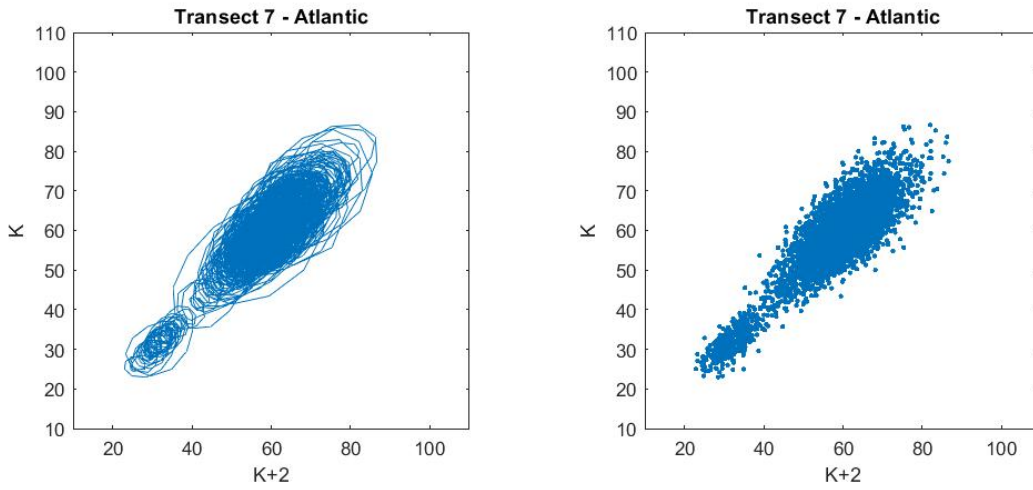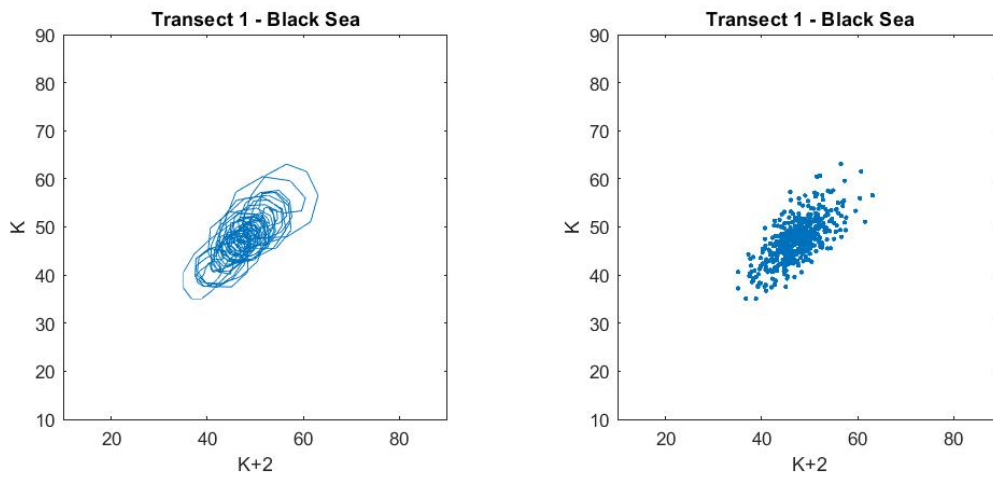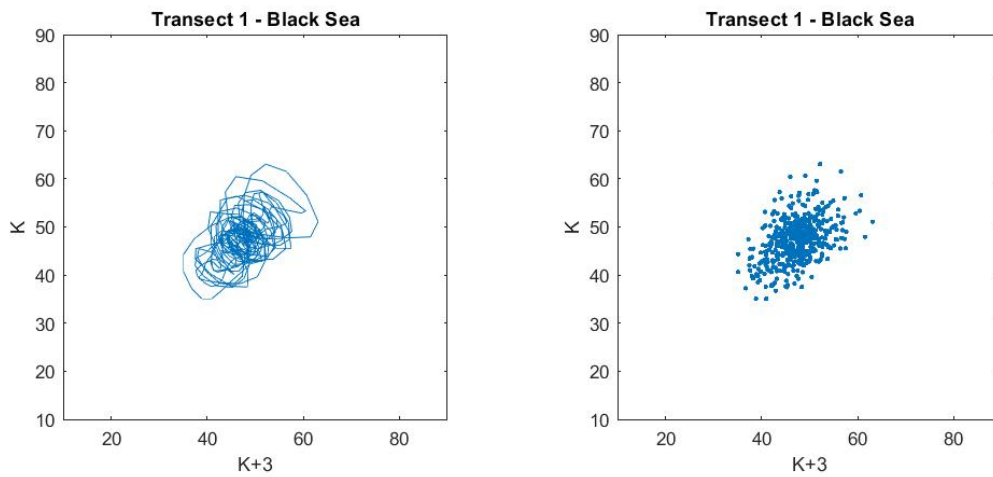
Figure 31- Lagged state space diagram DN(x) X DN(x+2)
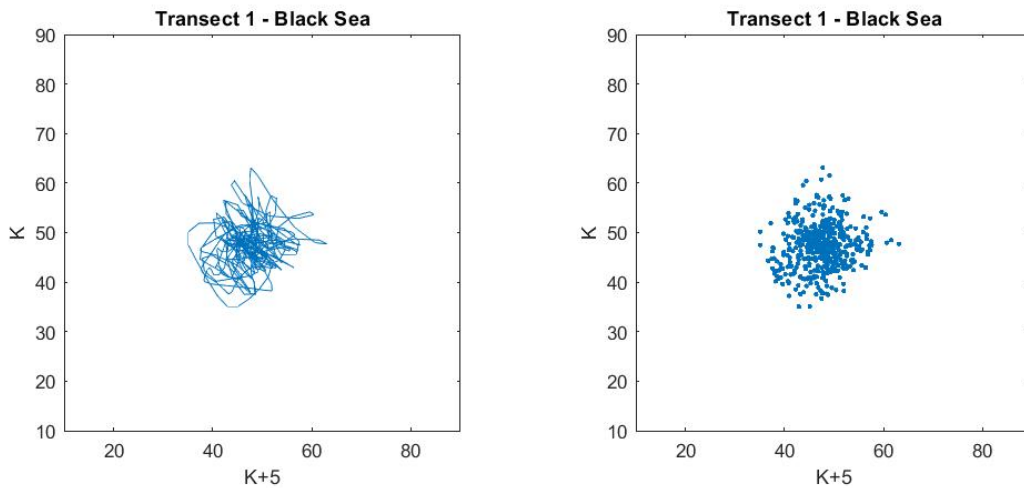

Figure 32- Lagged state space diagram DN(x) X DN(x+10)

Figure 33- Lagged state space diagram DN(x) X DN(x+100)

Figure 34- Lagged state space diagram DN(x) X DN(x+300)

3.1.2- Black-Sea

Transect lines crossing sea (Fig.35-39):

These transect lines have over 1600 pixels. The Bragg-type reflection explains why the majority of their grayscale values fall between 70 and 130 (Fig.35). In the representations of the lagged-space diagrams, the first DN(x) X DN(x+1) diagram displays a trend that approaches the correlation diagonal (Figure 38), and this trend may be detected faintly until the DN(x) X DN(x+3) diagram. Beginning with the DN(x) X DN(x+4) diagram, this geometric representation stabilizes and the dots tend to cluster around a center, close to the coordinates (100,100) (Fig. 39).
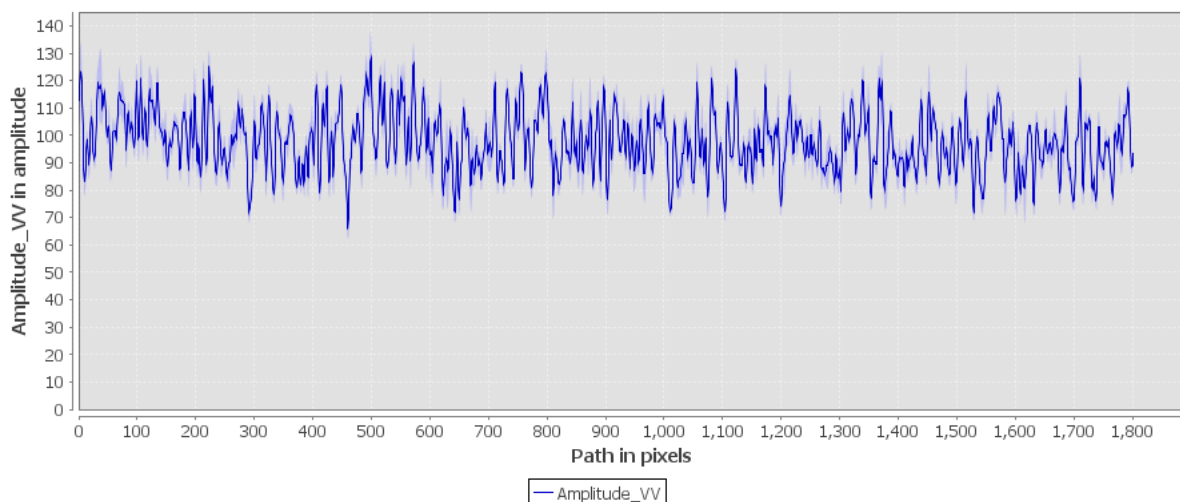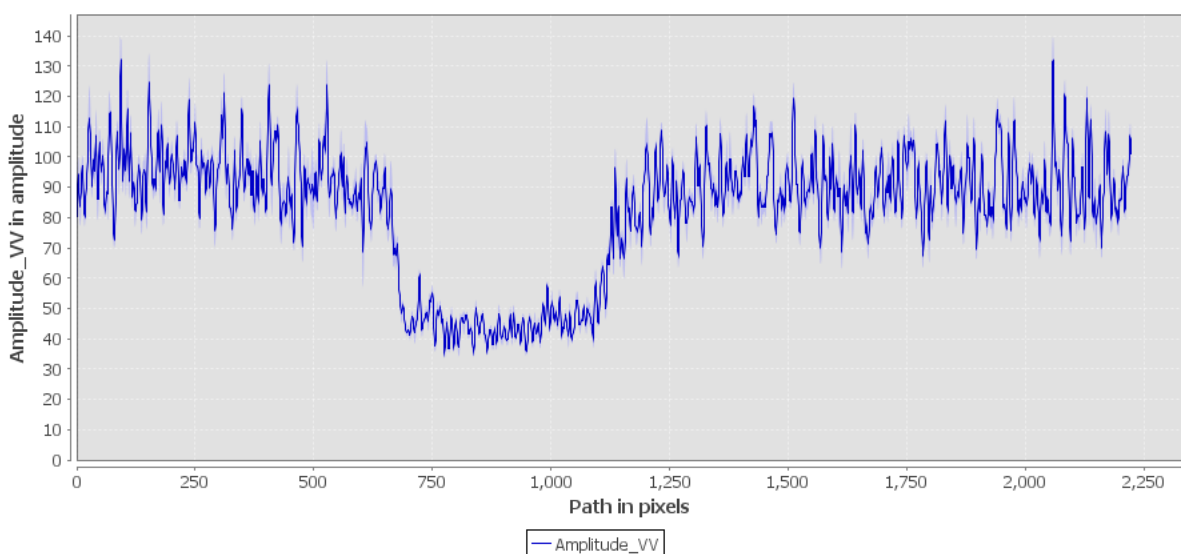

Figure 35- DN (x) values along transect line 5 in the Black Sea.
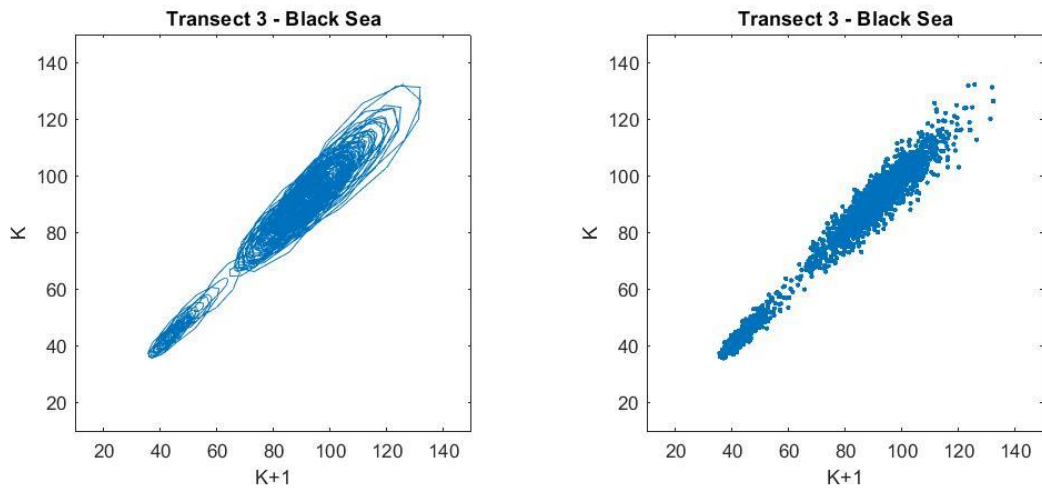
Figure 36- Lagged state space diagram DN(x) X DN(x+1)
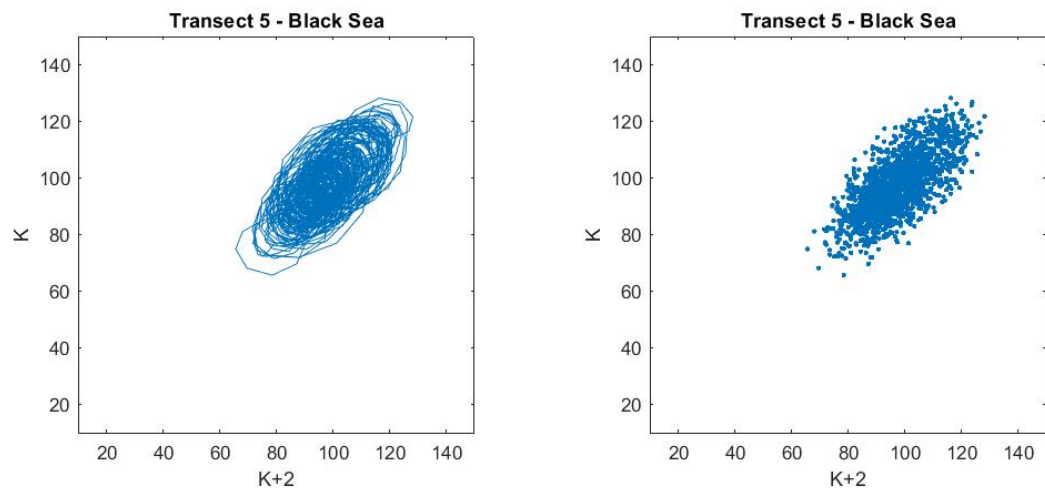
Figure 37- Lagged state space diagram DN(x) X DN(x+2)

Figure 38- Lagged state space diagram DN(x) X DN(x+3)

Figure 39- Lagged state space diagram DN(x) X DN(x+5)

Transect lines crossing oil (Fig. 40-44):

On the oil slicks, the transect lines contain around 500 pixels. As a result of the specular reflection from the oil spot, their gray level values are lower than in the ocean, with most amplitude values between 35 and 60.

Similar to the ocean, the tendency of the points in the lagged state diagrams is to migrate from the main diagonal to a cluster of points in the center (45,45) (Fig. 44). From k+4 diagram onward, the signature stabilizes.
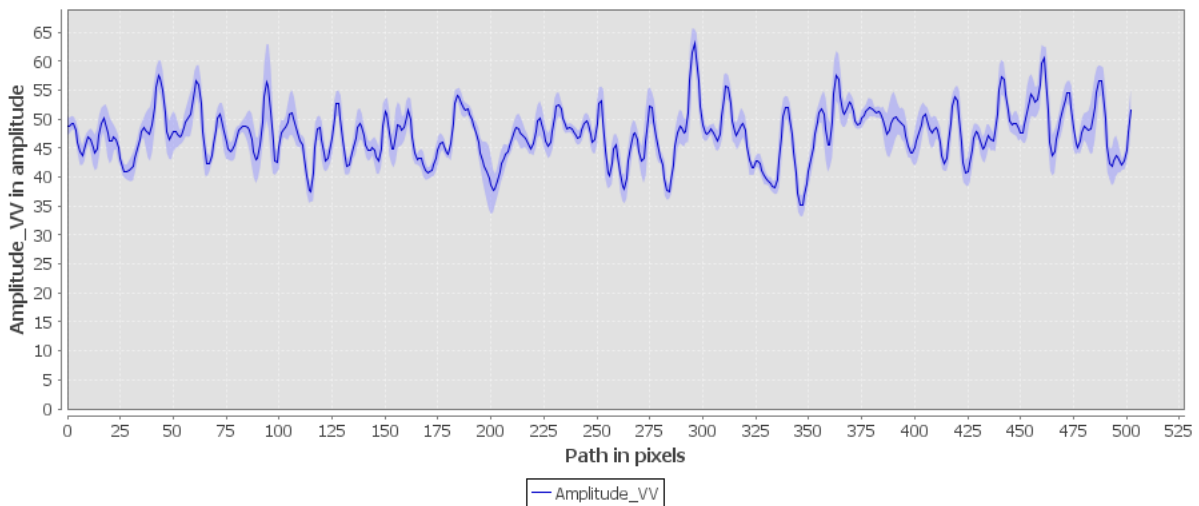
Figure 40- DN (x) values along transect line 1 in the Black Sea.
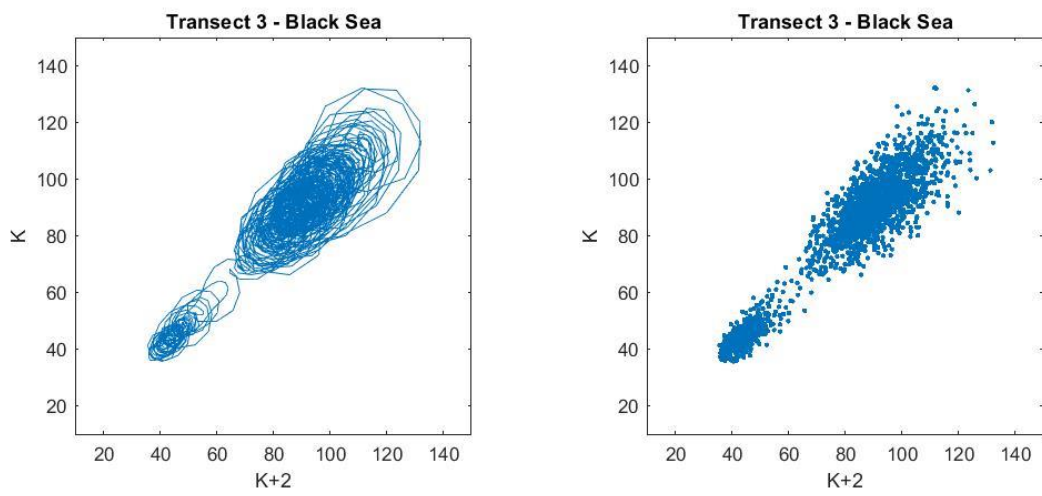
Figure 41- Lagged state space diagram DN(x) X DN(x+1)

Figure 42- Lagged state space diagram DN(x) X DN(x+2)

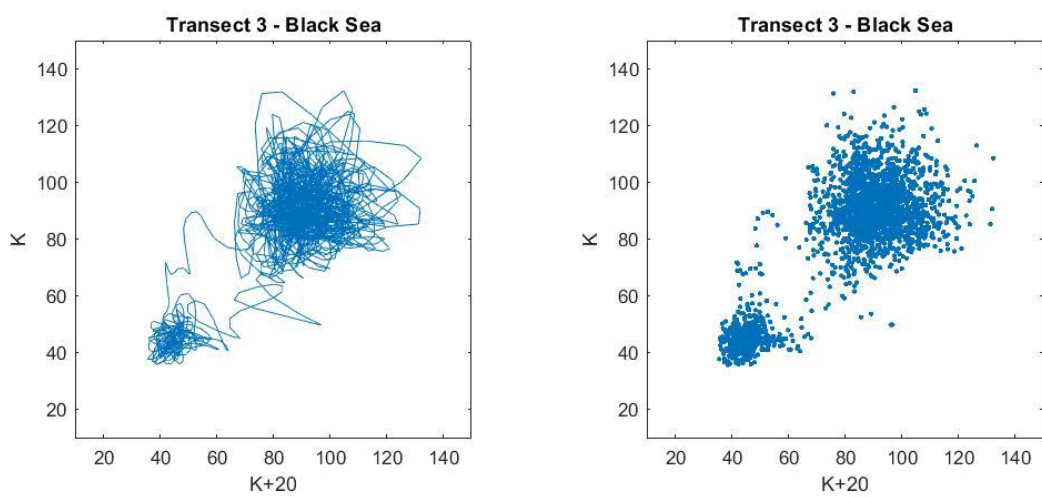Figure 43- Lagged state space diagram DN(x) X DN(x+3)

Figure 44- Lagged state space diagram DN(x) X DN(x+5)

Transect lines crossing sea and oil (Fig. 45- 49)

These Transect lines include more than 2,000 pixels and traverse both water and oil (Fig.45). Due to the different targets, their DN values vary considerably, with intermediate numbers connected with Bragg scattering and low values associated with the specular return from the oil. There are two foci for the lag DN(x+1), and both of them are on the correlation diagonal. For the delays from DN(x+4), we can detect two clusters with centers in the (30,30) and (60,60) coordinates, exhibiting a poor connection to the correlation diagonal (Fig.48).

A third cluster with coordinates (45,45) can be distinguished with the passage of time lags. As seen in the k+100 plot, there was a posterior migration of the points in the lower portion of the plot with values between (30, 40-60) (Fig.49).

Figure 45- DN (x) values along transect line 3 in the Black Sea/

Figure 46- Lagged state space diagram DN(x) X DN(x+1)

Figure 47- Lagged state space diagram DN(x) X DN(x+2)
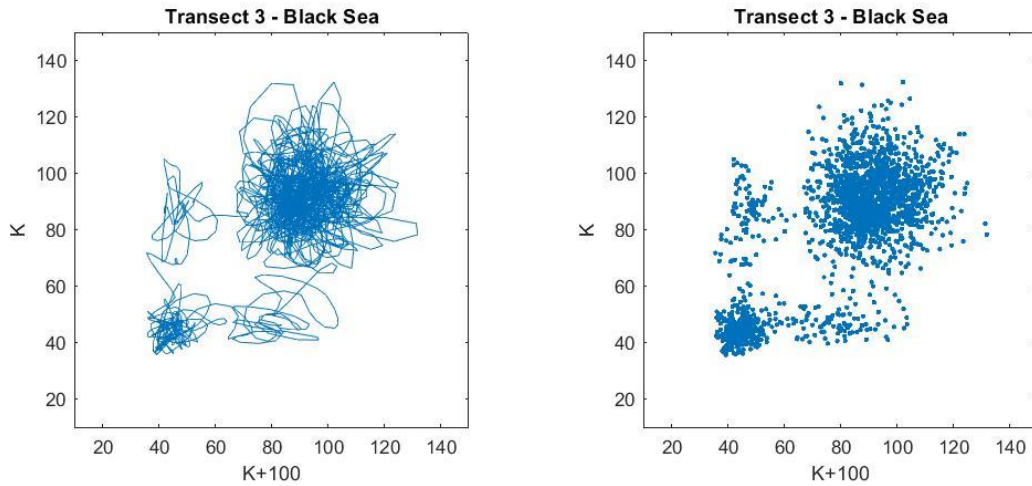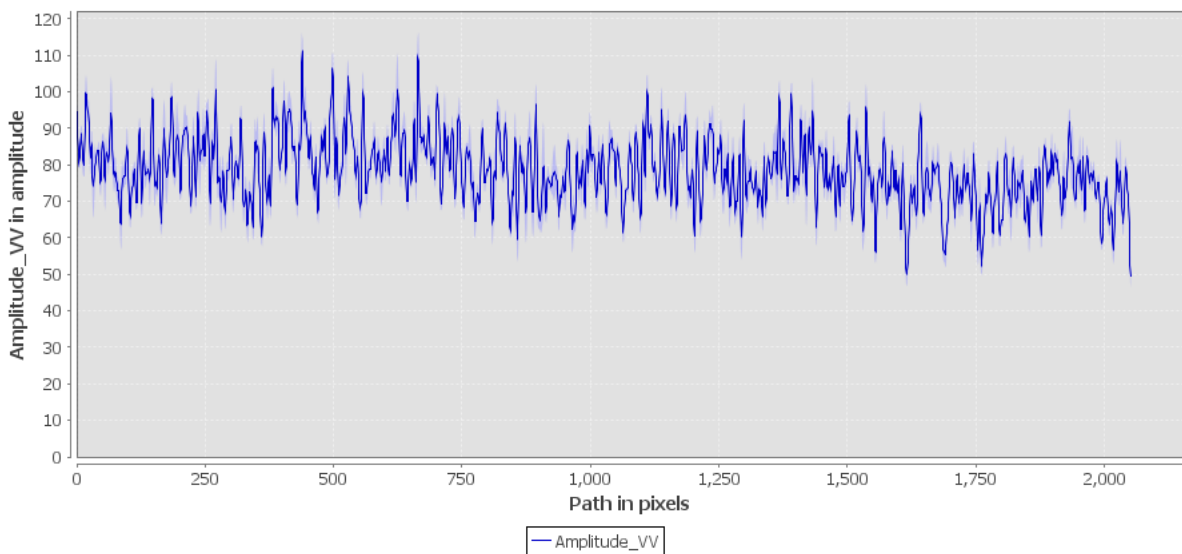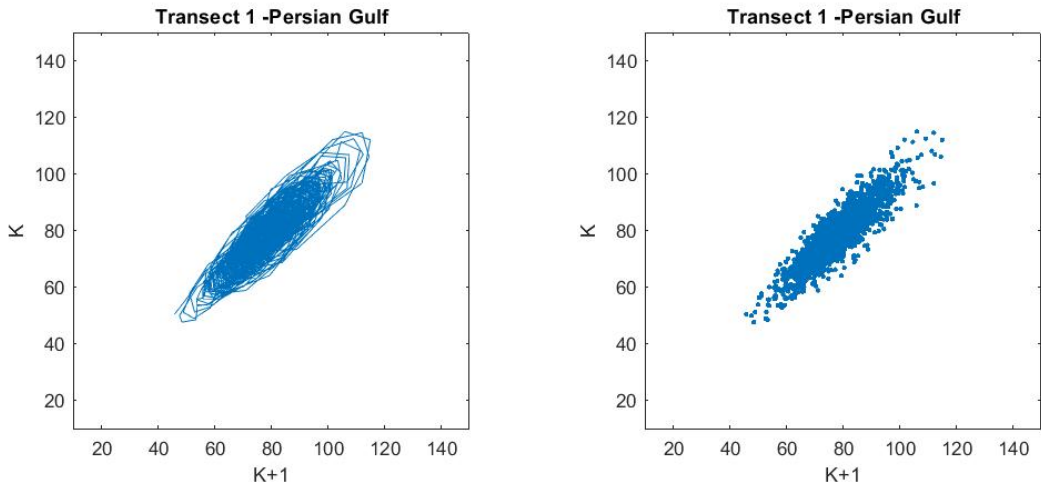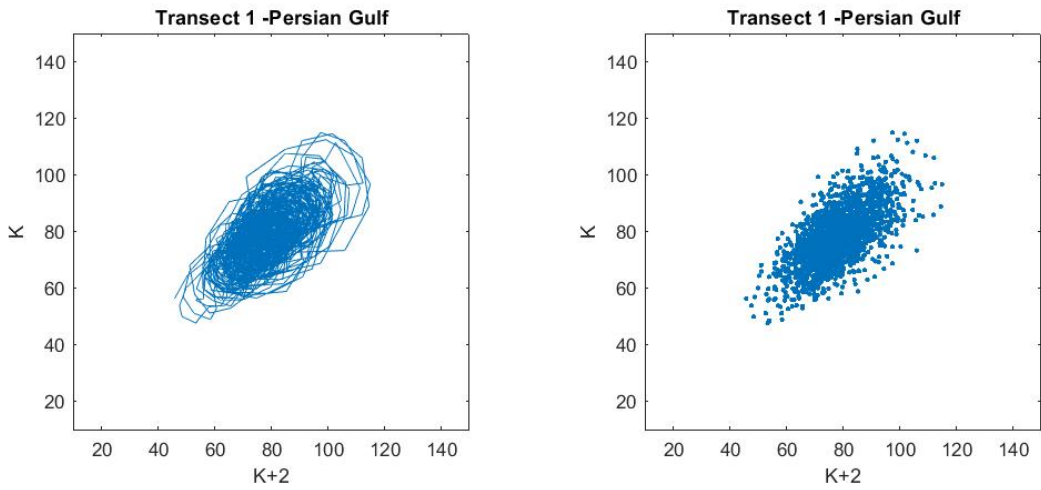

Figure 48- Lagged state space diagram DN(x) X DN(x+20)

Figure 49- Lagged state space diagram DN(x) X DN(x+100)

3.1.3- Persian Gulf

Transect lines crossing Sea (Fig.50-54)

These transect lines have over 1300 pixels. Due to the Bragg-type reflection the majority of their grayscale values fall between 70 and 130 (Fig.50). In the representations of the lagged-space diagrams, the first DN(x) X DN(x+1) diagram displays a trend that approaches the correlation diagonal (Fig.51), and this trend may be detected faintly until the DN(x) X DN(x+3) diagram. Beginning with the DN(x) X DN(x+4) diagram, this geometric representation stabilizes and the dots tend to cluster around a center, close to the coordinates (80,80) (Fig. 54).

Figure 50- DN (x) values along transect line 1 in the Persian Gulf.

Figure 51- Lagged state space diagram DN(x) X DN(x+1)

Figure 52- Lagged state space diagram DN(x) X DN(x+2)

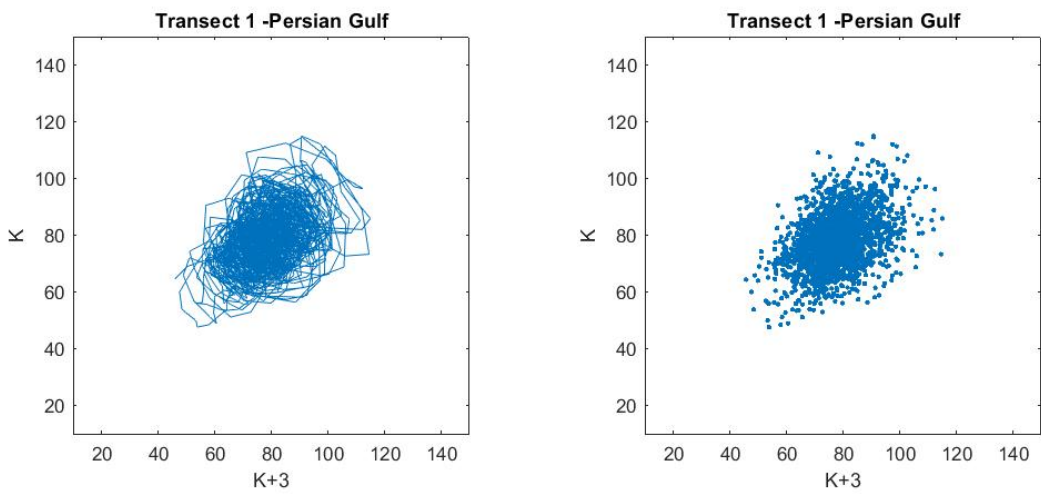

Figure 53- Lagged state space diagram DN(x) X DN(x+3)
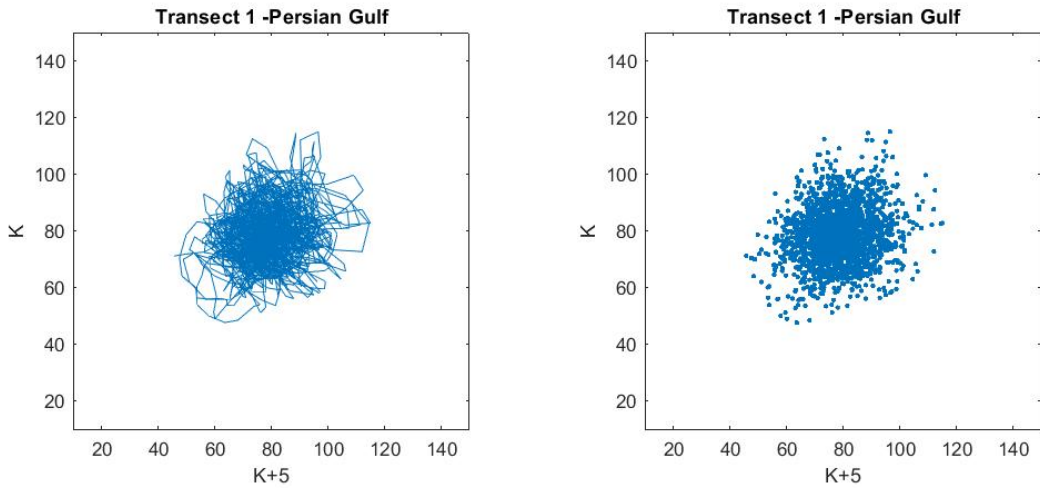
Figure 54- Lagged state space diagram DN(x) X DN(x+5)

Transect lines crossing oil (Fig 55-58):

On the oil slicks, the transect lines contain between 190 e 600 pixels (Fig.55). As a result of the specular reflection from the oil spot, their gray level values are lower than in the ocean, with most amplitude values between 35 and 55.

Similar to the ocean, the tendency of the points in the lagged state diagrams is to migrate from the main diagonal to a cluster of points in the center (45,45) (Figure58). From k+3 diagram onward, the signature stabilizes.
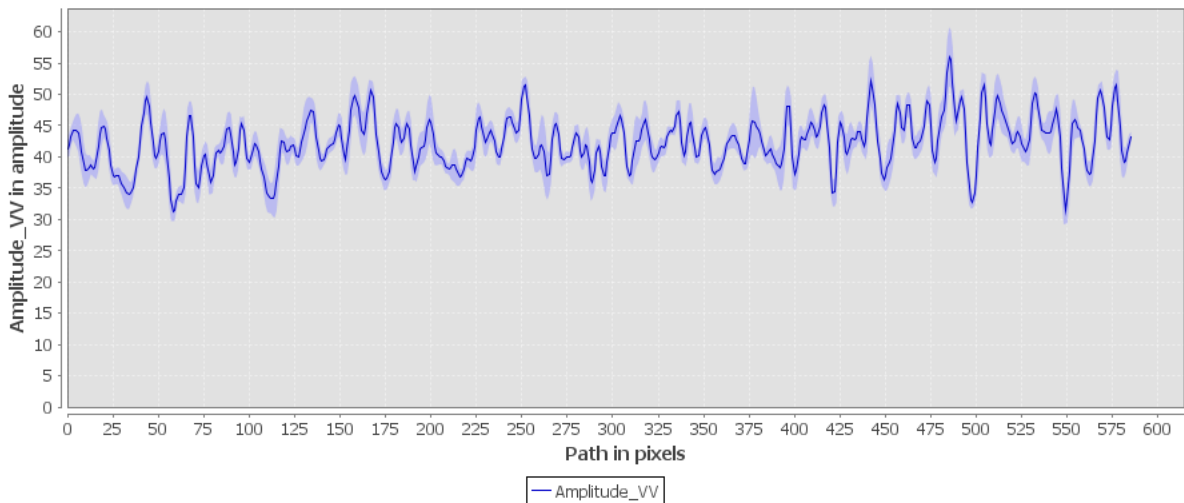

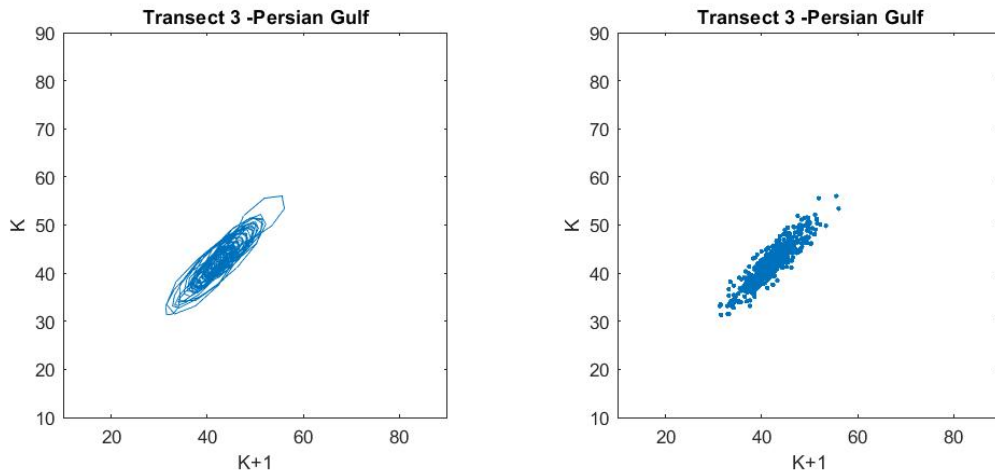Figure 55- DN (x) values along transect line 5 in the Persian Gulf.
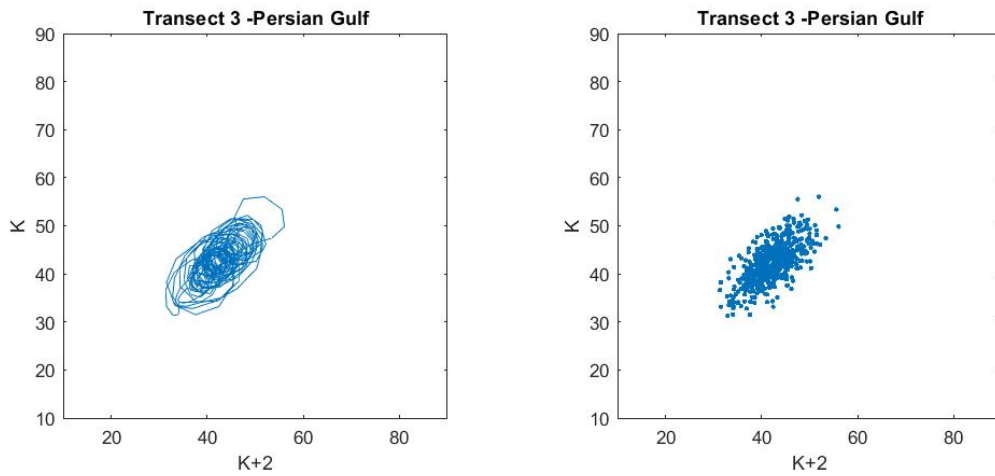
Figure 56- Lagged state space diagram DN(x) X DN(x+1)
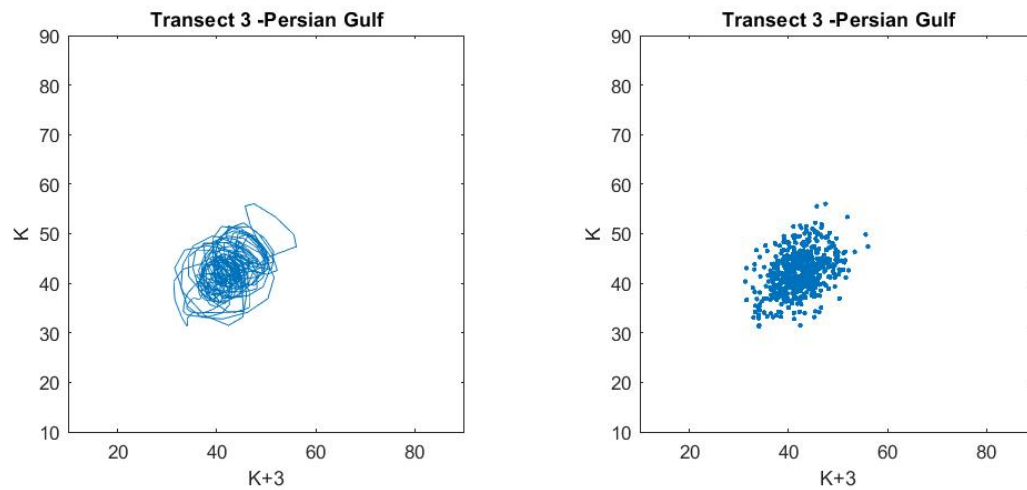

Figure 57- Lagged state space diagram DN(x) X DN(x+2)

Figure 58- Lagged state space diagram DN(x) X DN(x+3)

Transect lines crossing false alarm (Fig.59-66)

The Transect lines over the false alarm are comprised of between 71 and 575 pixels (Fig.59). The same way as the ocean and oil in the first two lags, DN(x+1) and DN(x+2), points on the preferential diagonal are evident (Fig.60). In later figures, the cluster is no longer elongated and becomes centered at (42,42), and from k+5 onwards, it is somewhat squared and more angular than the oil cluster (Fig. 62-66). This target's gray level values are low, ranging between approximately 35 and 50 (the same as the oil values).
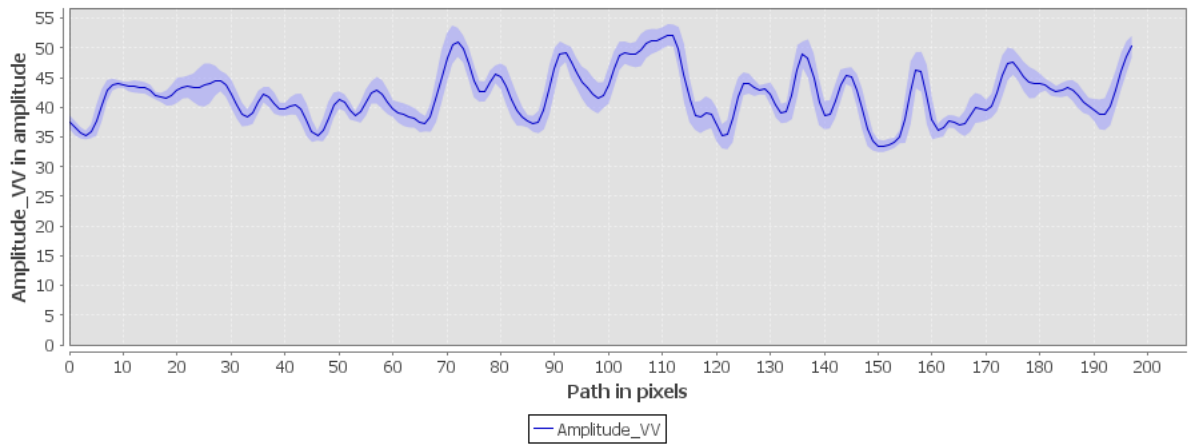

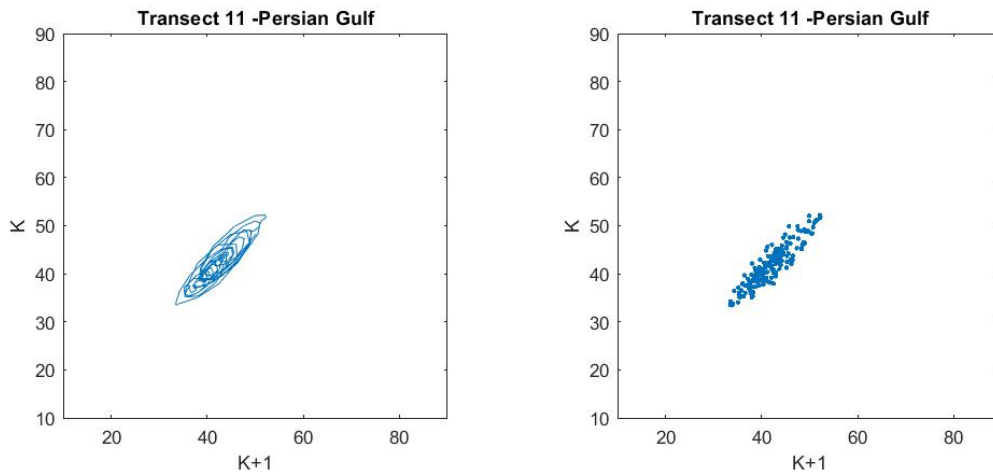Figure 59- DN (x) values along transect line 11 in the Persian Gulf.
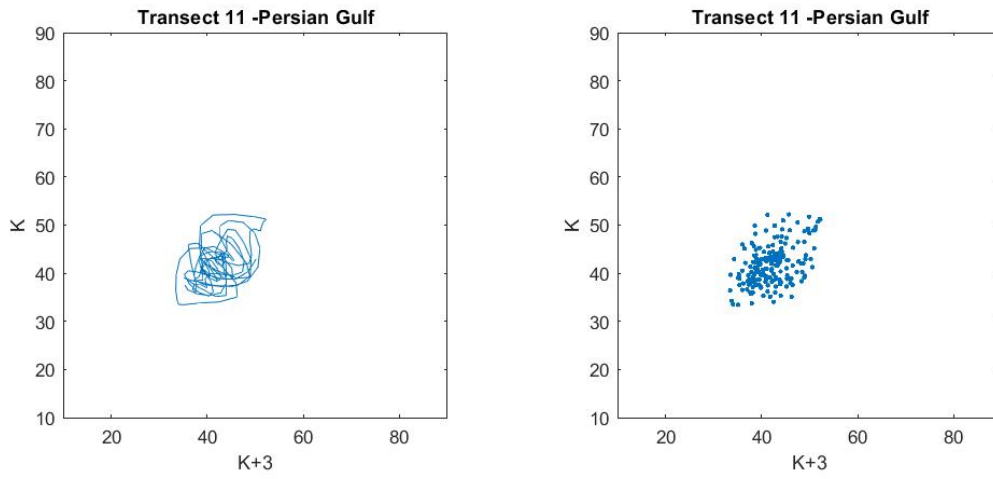

Figure 60- Lagged state space diagram DN(x) X DN(x+1)

Figure 61- Lagged state space diagram DN(x) X DN(x+3)
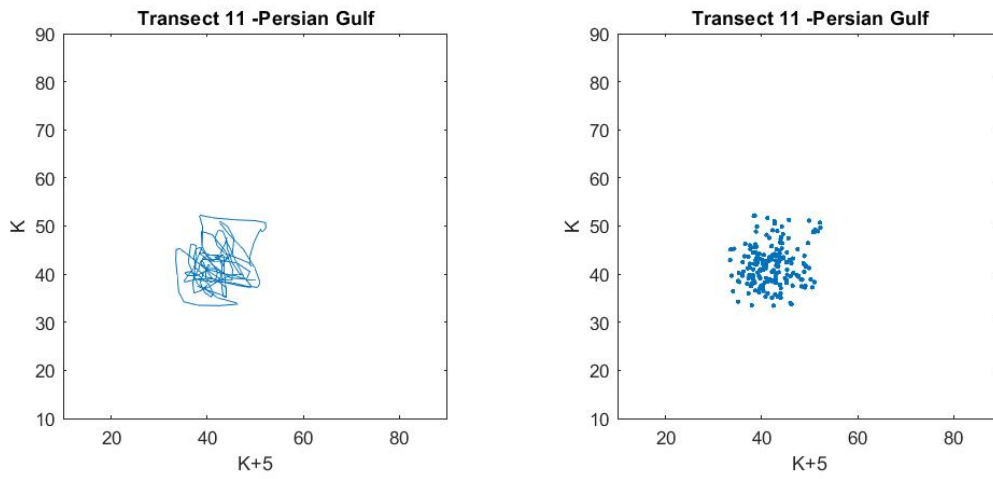

Figure 62- Lagged state space diagram DN(x) X DN(x+5)
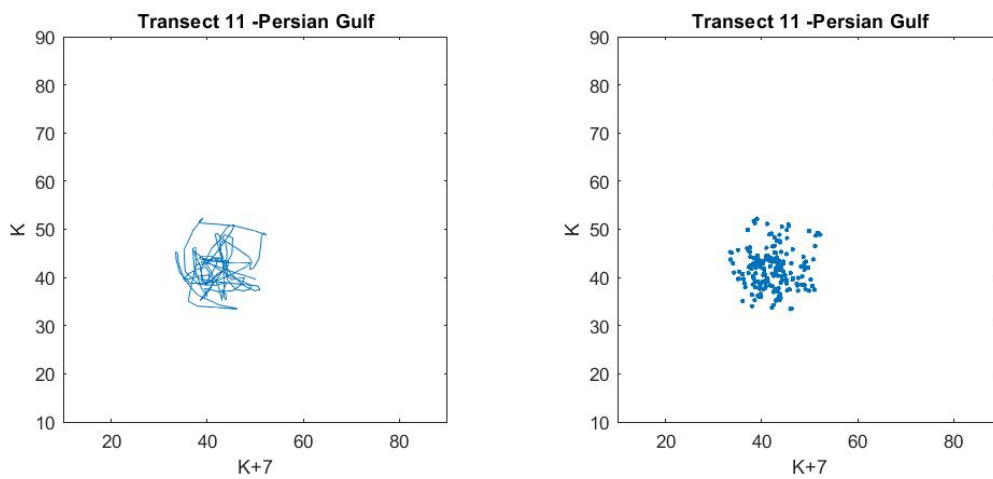

Figure 63- Lagged state space diagram DN(x) X DN(x+7)

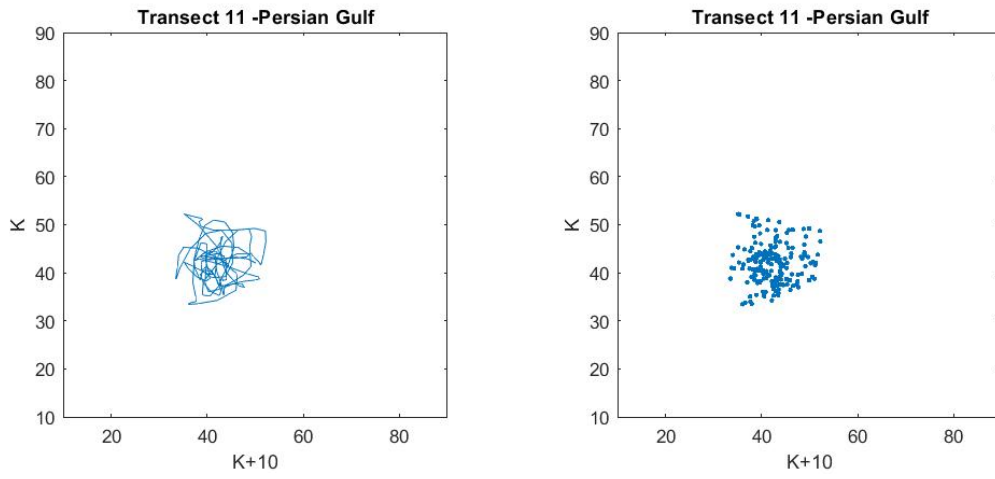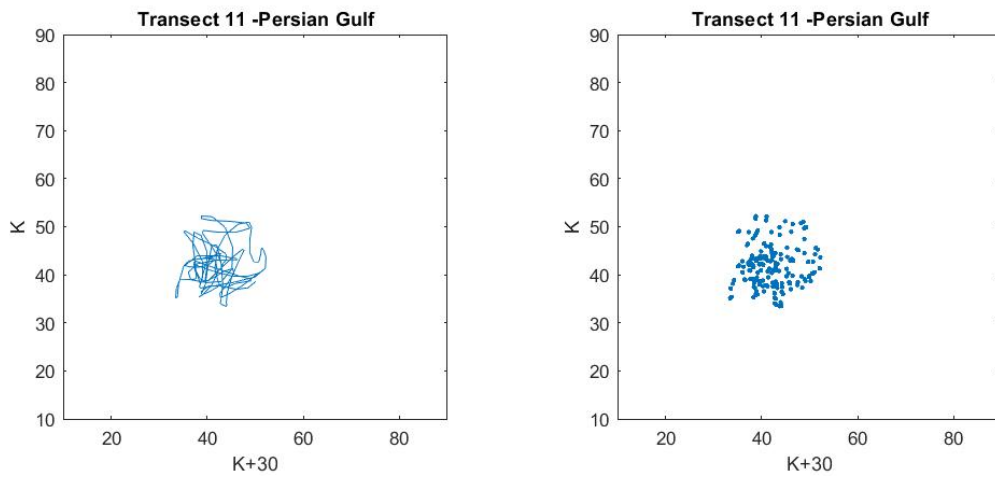Figure 64- Lagged state space diagram DN(x) X DN(x+10)
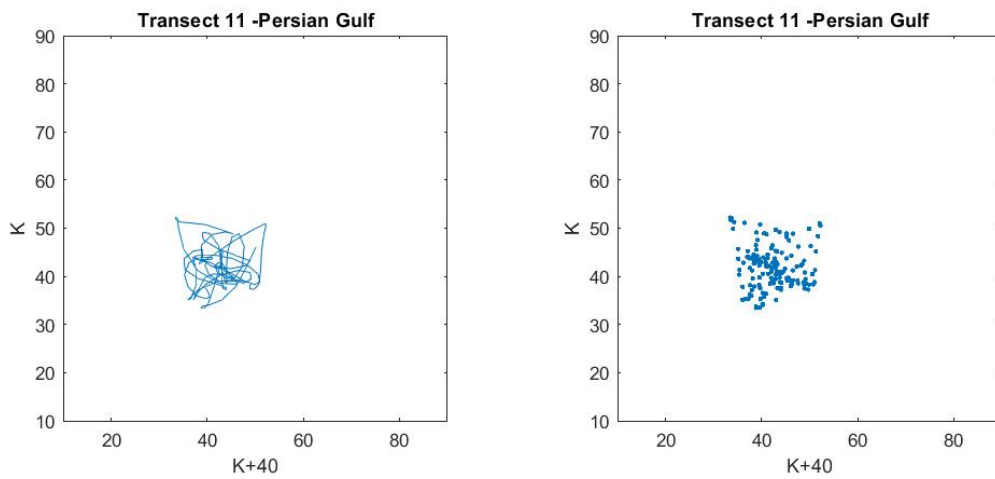

Figure 65- Lagged state space diagram DN(x) X DN(x+30)

Figure 66- Lagged state space diagram DN(x) X DN(x+40)

Transect lines crossing the Sea and oil (Fig.67-73):

These Transect lines include more than 2,000 pixels and traverse both water and oil (Fig.67). Due to the different targets, their DN values vary considerably, with intermediate numbers connected with Bragg scattering and low values associated with the specular return from the oil. There are two foci for the lag DN(x+1), and both of them are on the correlation diagonal. For the delays from DN(x+4), we can detect two clusters with centers in the (40,40) and (80,80) coordinates, exhibiting a poor connection to the correlation diagonal.

As the shifts continue, the points migrate horizontally and vertically in the directions (40,80) and (80,40) (Fig.72).

At k+500, it is clearly seen that there is a clearly defined region in the lower right corner of the created square signature that is not occupied by points (Fig.73).

Figure 67- DN (x) values along transect line 9 in the Persian Gulf.
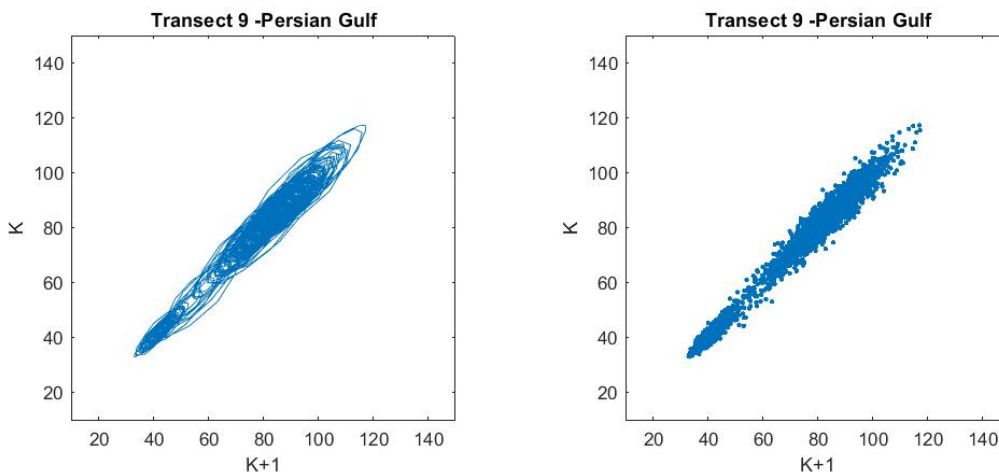
Figure 68- Lagged state space diagram DN(x)X DN(x+1)

45

Figure 69- Lagged state space diagram DN(x) X DN(x+2)

Figure 70- Lagged state space diagram DN(x) X DN(x+3)

Figure 71- Lagged state space diagram DN(x)X DN(x+50)

Figure 72- Lagged state space diagram DN(x) X DN(x+100)

Figure 73- Lagged state space diagram DN(x) X DN(x+500)

Transect lines crossing the Sea and false target (Fig.74-81)

These Transect lines comprise between 2677 and 2841 pixels and traverse the ocean and false alarm (Fig.74). Due to the diversity of targets, their DN values range widely between 30 and 150. For the DN(x+1) lag, an alignment with the correlation diagonal is observed. This alignment persists until approximately k+50 (Fig.79). With the progression of the lags, a horizontal and vertical migration of the points happens to the horizontal and vertical directions surrounding the core cluster at (85,80) creating a square likely figure.

At DN(x+50), a primary cluster is still visible, but the entire region (approaching a square) is occupied by the points with abscissae at 40 and 120.
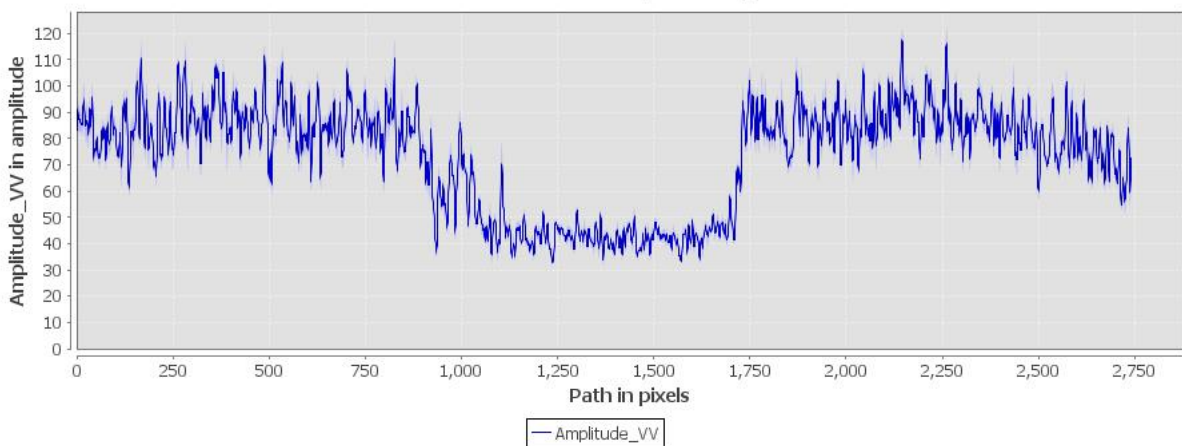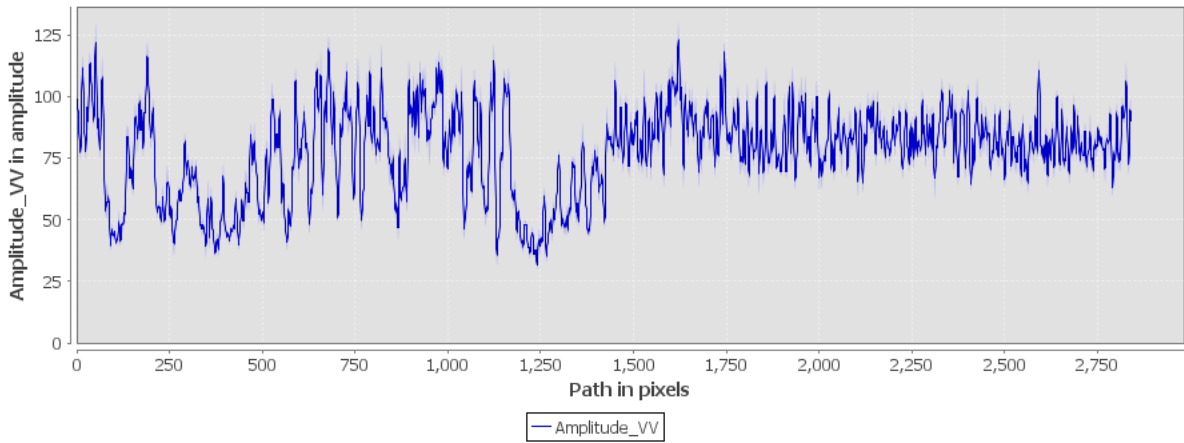
Figure 74- DN (x) values along transect line 19 in the Persian Gulf.
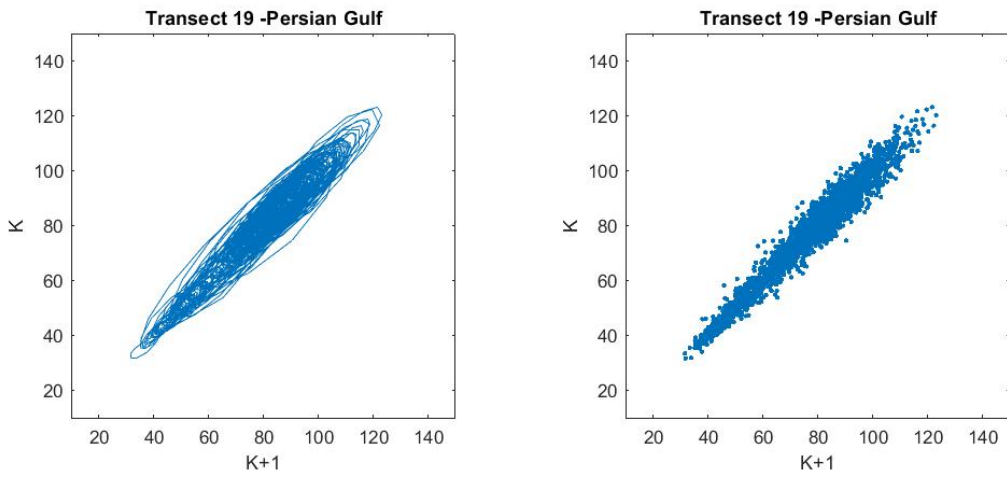
Figure 75- Lagged state space diagram DN(x) X DN(x+1)
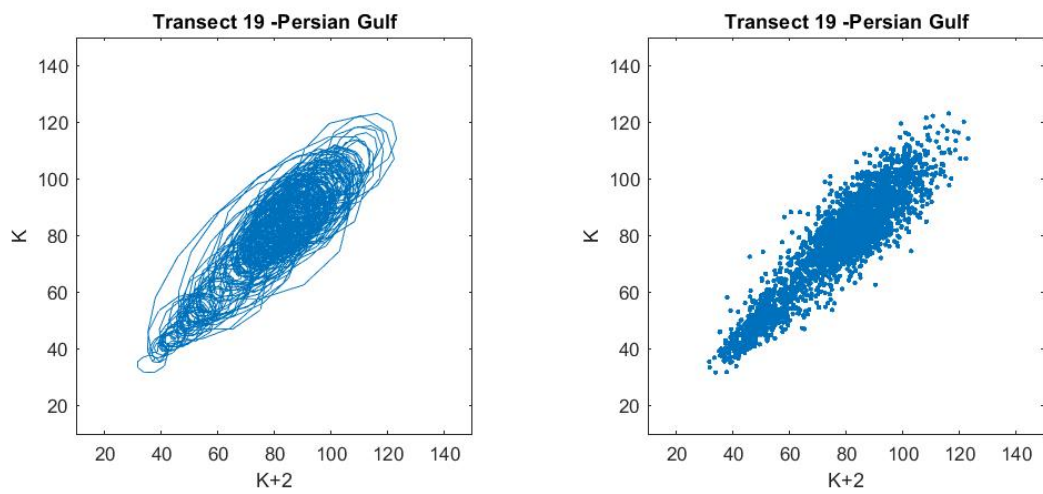
Figure 76- Lagged state space diagram DN(x) X DN(x+2)
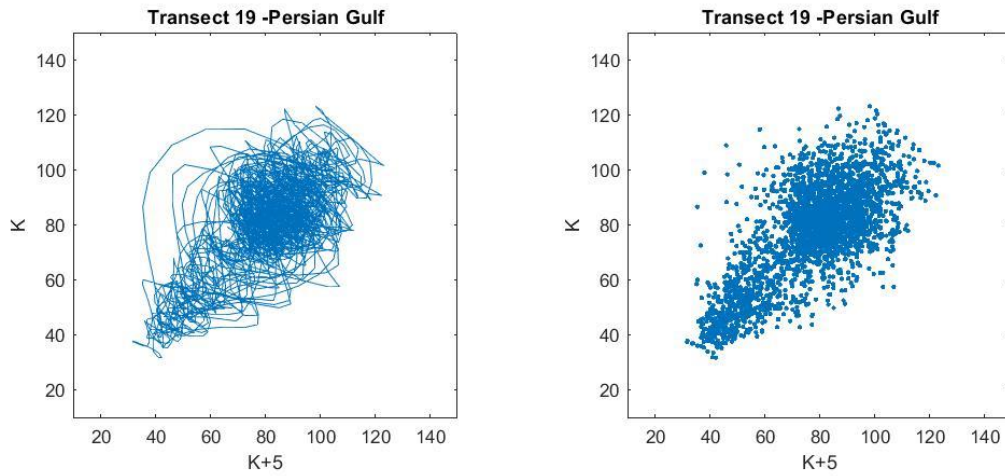
Figure 77- Lagged state space diagram DN(x) X DN(x+5)
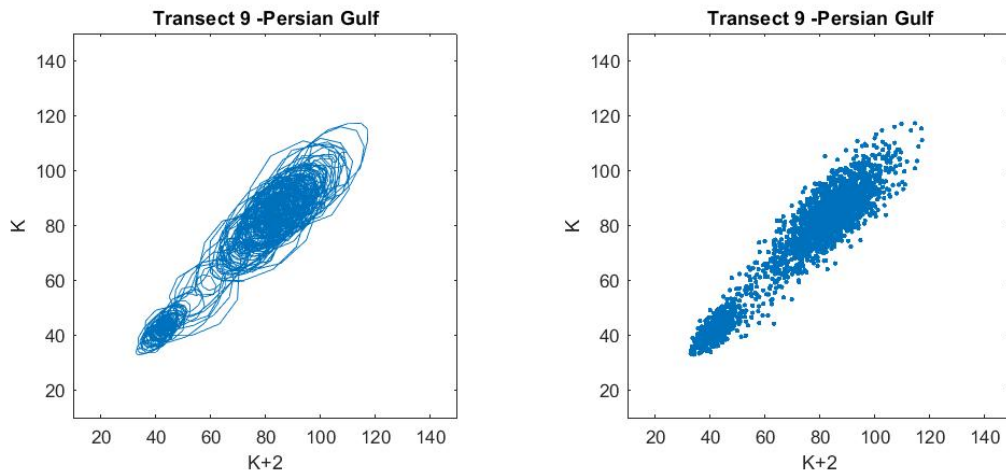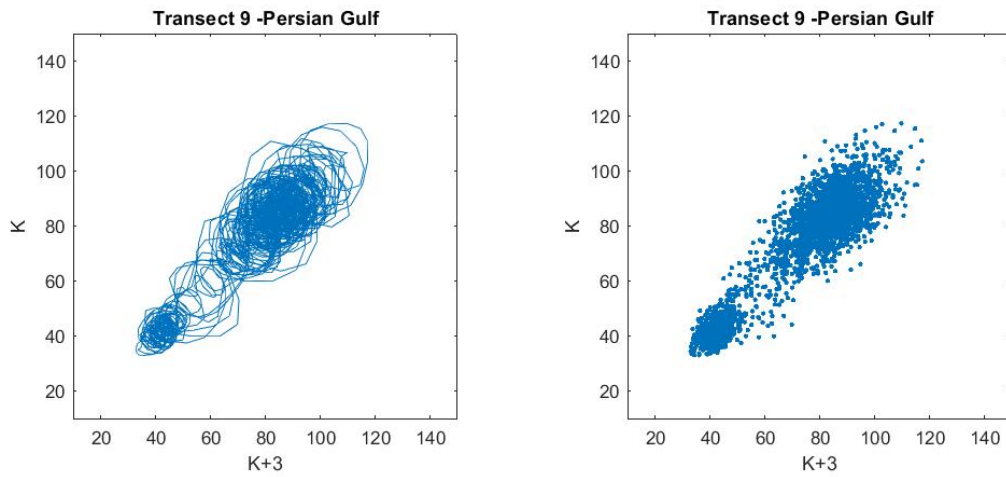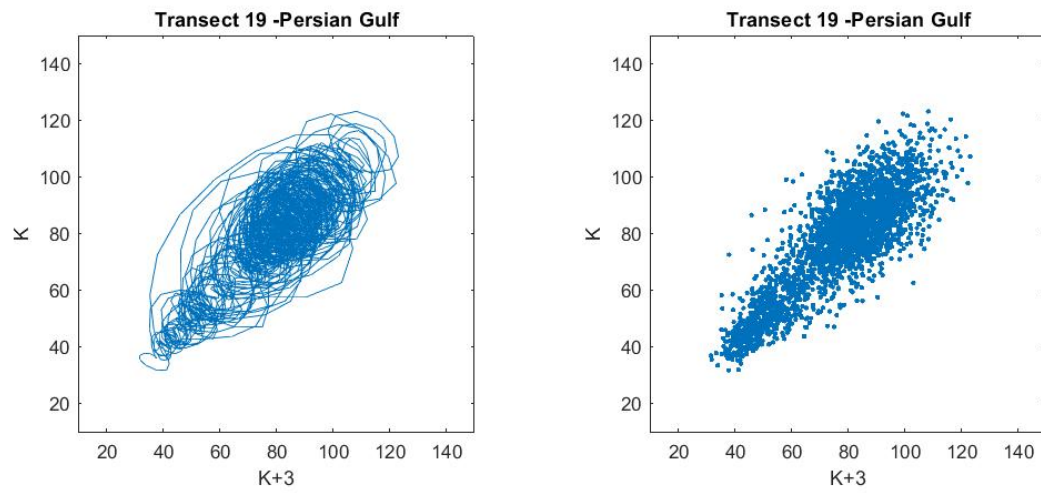

Figure 78- Lagged state space diagram DN(x) X DN(x+3)
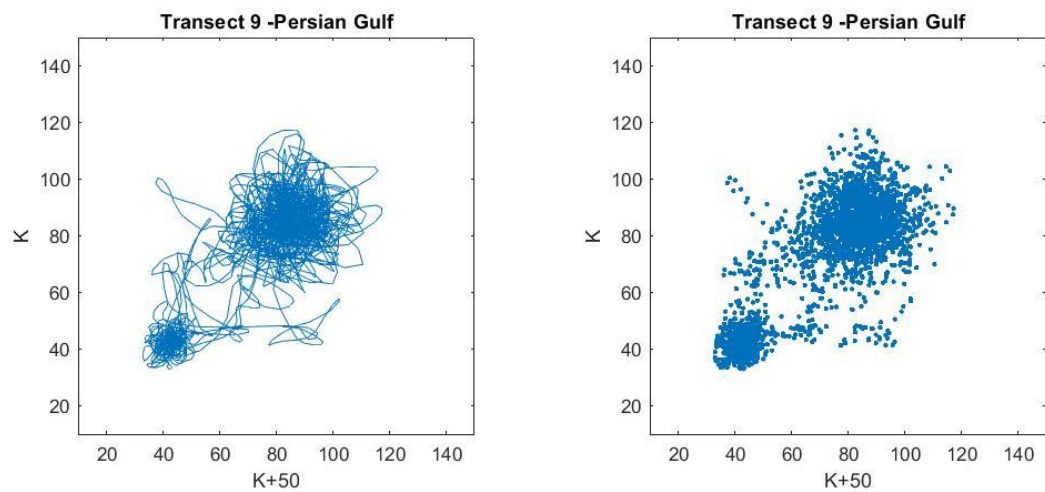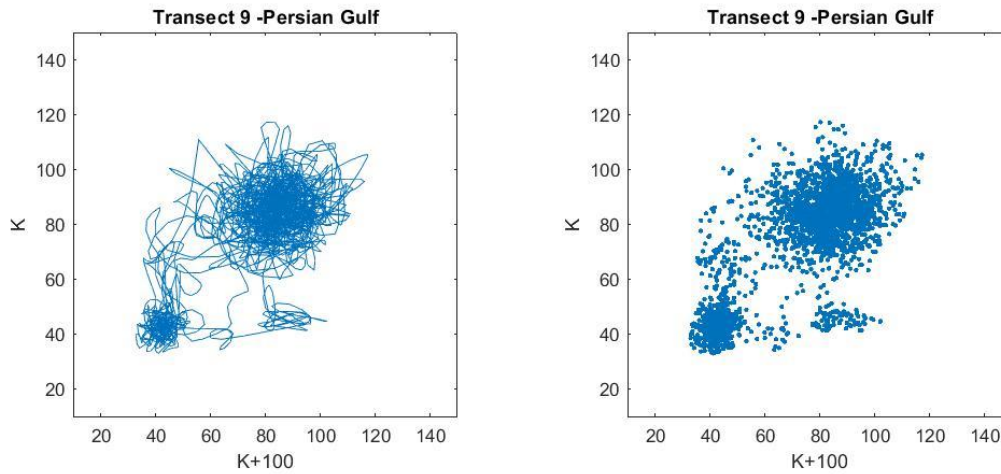

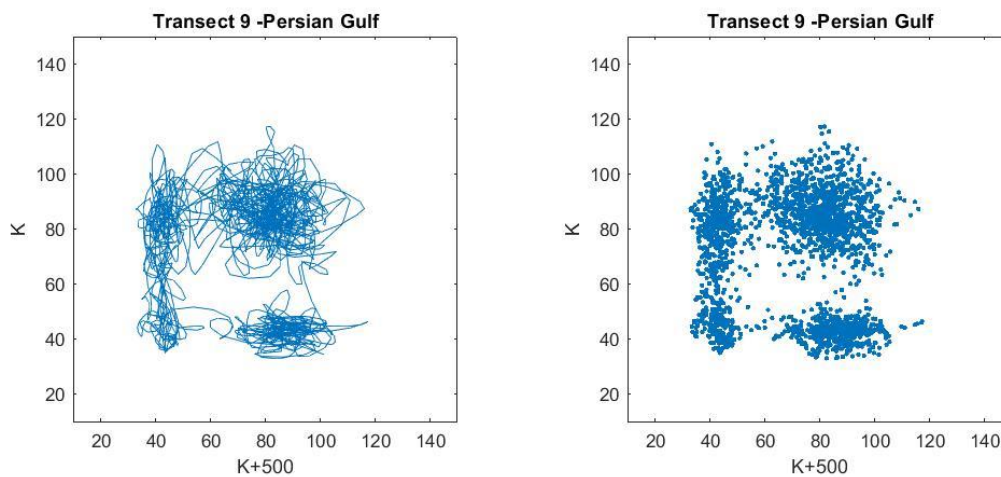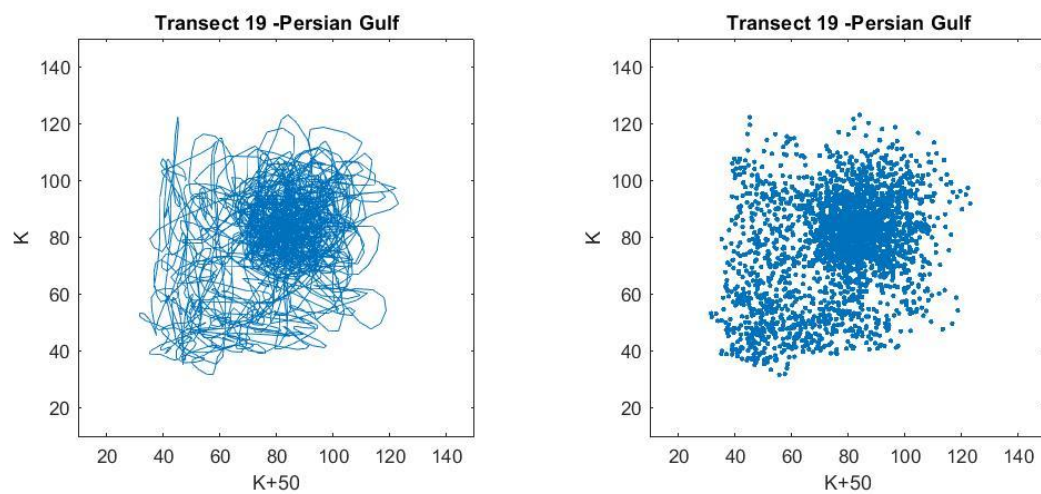Figure 79- Lagged state space diagram DN(x)X DN(x+50)
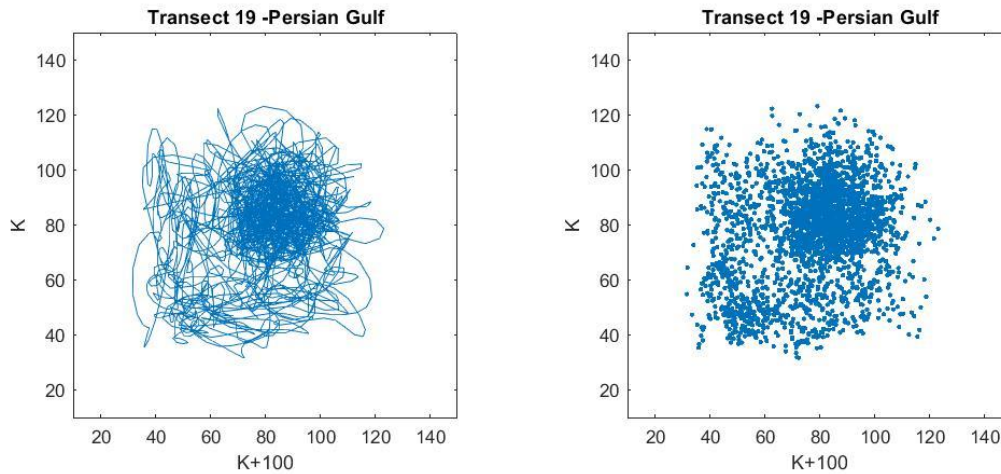
Figure 80- Lagged state space diagram DN(x)X DN(x+100)
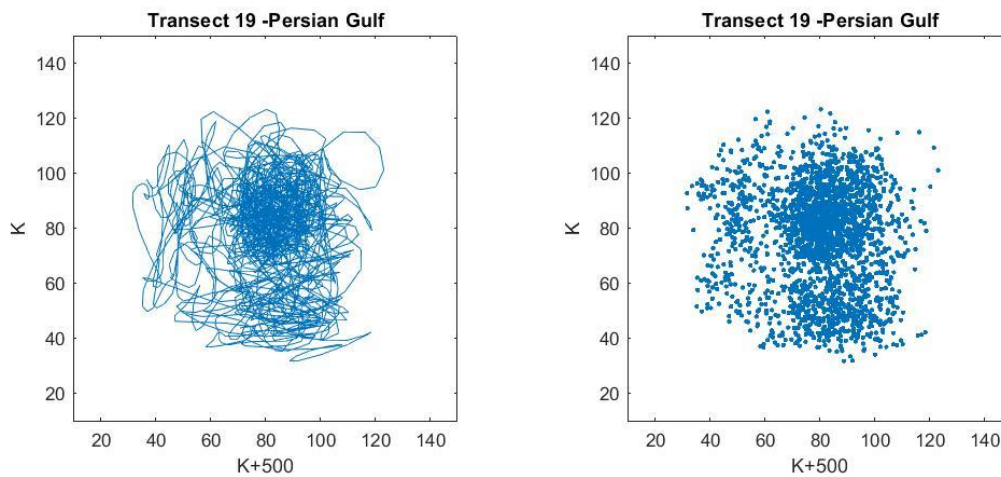
Figure 81- Lagged state space diagram DN(x)X DN(x+500)

3.2- Discussion

The outputs of the lagged state space diagrams allow the identification of specific patterns and signatures associated with each target type. It is easy to see within the diagrams that there are preferential areas of point occupancy as well as restricted locations, where the points do not occupy.

No significant differences can be observed between the horizontal and vertical transects.

When studying the space-lagged diagrams of the ocean, it is possible to observe a common feature shared by all of the studied images: a migration of the points away from the preferential diagonal and into a cluster of points. This conglomerate displays different values of digital numbers depending on the ocean and the image that is being examined.

Atlantic: (65,70)

Black Sea: (100,100)

Persian Gulf: (80,80)

It is evident that the behavior of the ocean is remarkably similar to that observed in the Gulf of Mexico using RADARSAT1, however presenting lower gray levels. In the case of RADARSAT, the ocean shows a cluster of points centered at (80,80). This is to be expected given that the acquisition angle and electromagnetic wave pulse size employed by the two distinct radar systems are distinct.

By analyzing the oil transects, it can be seen that the oil behaves quite similarly to the ocean, in contrast to what was observed by the study using RADARSAT.

The points migrate to a cluster with centers at lower values bounded between (35,35) and (45,45):

Pacific: (35,35)

Black Sea (45,45)

Persian Gulf: (42,42)

This behavior is intriguing, as a significant portion of the reflection returns to the sensor despite the oil's tendency to specular backscatter.

As far as RADARSAT is concerned, the values obtained would be close to zero or zero.

Analyzing the transects that pass through sea and oil, it is evident that the state-spaces evolve from the correlation diagonal to two main areas, the centers of this areas present coordinates close to the centers of the clusters obtained by the sea and oil separately. The signature evolves to a slightly square shape feature with an empty area in the lower left center.

The false alarm target studied in the image of the Persian Gulf evolves similarly to the oil, but has a somewhat squared cluster structure. The central coordinates location is identical to the location of the oil. Although a variation is detected, it is not as distinct as the difference observed on the RADARSAT image, in which the false target prefers to occupy a narrow region to the lower left starting from the coordinate (0,0).

When analyzing "oil and sea" and "false alarm and sea" it is important to note that the signatures are quite distinct.

It can be seen that in both cases there is a tendency for a creation of a major cluster of points, but only with the false alarm the entire area (approaching a square) is occupied by the points with abscissae at 40 and 120, with no empty regions.

In light of the outcomes, it is evident from this investigation that signatures associated with lagged state spaces diagrams can be identified.

When compared to RADARSAT1, the SENTINEL1 has a reduced identification potential due to a lower contrast between the digital numbers from the different targets. The oil exhibits mainly null values in RADARSAT, and it's values tend to go migrate to the axes of the diagrams, positively impacting on the oil identification since it can be more easily distinguished from the false alarm. Although it is feasible to observe a tendency of the false alarm signatures when utilizing SENTINEL 1, it is a tougher differentiation since the characteristics are quite similar to the oil signature. (fig.81)
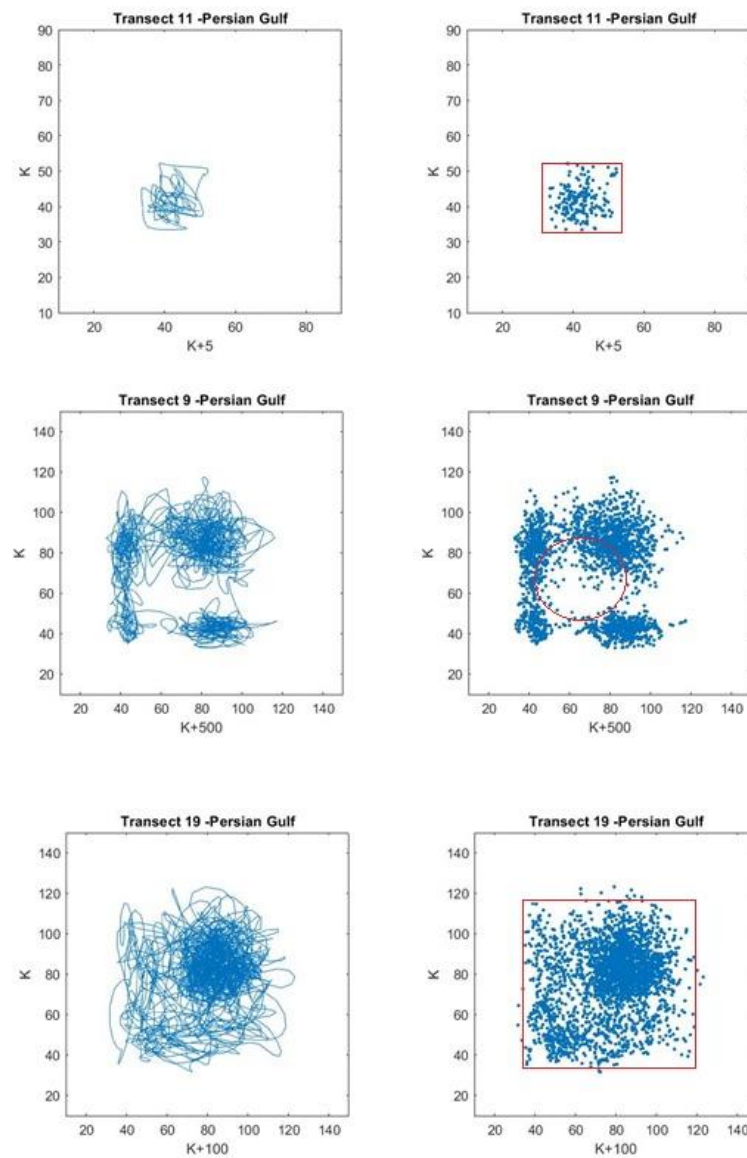

Figure 81- Diagrams featuring false alarm, "sea and oil" and "sea and false target".

Different conditions at sea will affect the backscattering and, consequently, the DN. However, despite the differences in locations and images, the trajectories observed in the diagrams and migration of the points are consistent, being a good indicator for the potential application of this method in order to identify oil on the ocean surface.

The signatures formed by transects that traverse "sea and false alarms" are highly promising; a large area that tends toward a square shape is filled by the points, and when compared to the "sea and oil signature", it is noticeable an area within this square that is never occupied by the dots.

Recommendations: For this type of application, RADARSAT is preferred because the contrast between oil and water is generally greater. This is primarily attributable to the acquisition angle and the wave's amplitude. However, with the help of SENTINEL1, it is possible to distinguish false targets from real ones, particularly when contrasting the characteristics of sea and oil with those of sea and false alarm.

Conclusion

The challenge connected with the identification of oil slicks by SAR is caused by uncertainties in the interpretation of the image, known as false alarms, which exhibit similar backscattering characteristics to those of the oil at sea, making its surveillance difficult.

In light of the requirement for ongoing monitoring in cases of marine exudations or oil spills, the suggested technique intends to increase the speed and decrease the subjectivity of the identification process of oil, using SAR images, without the use of more complex data.

The methodology employs lagged state space diagrams constructed with the values of the image's transect lines, which pass through the sea, oil, and a false target.

This technique is promising, since the trajectories generated in the diagrams are representative of each target type, the sea displays a very characteristic and consistent trajectory, and different signatures were formed for oil and the false target, permitting their differentiation:

Sea: The trajectory in the diagrams evolves into a cluster of dots.

Oil: Similar to sea, but with less gray numbers.

False alarm: A minor preferential square area of the points is defined, nevertheless with values extremely similar to those of the oil.

Oil and sea: The dots occupy a large, distinct area, migrate horizontally and vertically, and do not occupy a portion of the diagram.

False target and sea: a square-shaped area resembling "oil and sea" is occupied, but there are no empty places in the diagram's center.

Therefore, it can be concluded that the trajectories created by the lagged state diagram are diagnostic for the various target kinds.

Taking into account the previously performed work, for this type of application, RADARSAT is preferred because the contrast between oil and water is generally greater. However, with the help of SENTINEL1, it is possible to distinguish false alarms from oil, particularly when contrasting the characteristics of sea and oil with those of sea and false target.

For the advancement of this research, it would be beneficial to conduct additional testing on other images and false alarms. This would help validate and expand this new method for identifying oil spills. In the long run, it might be possible to automate the process of making diagrams and analyzing them.

Bibliography

Andrade, N. S. O., Rosa, A. N. C. S., & Faria, P. C. C. (2007, April). Fundamentos de Polarimetria SAR. INPE/Simpósio Brasileiro de Sensoriamento Remoto, 4775–4782.

Ascom Ufal. (2019, November 14). Lapis alerta que mais um satélite detectou grande vazamento de óleo. Universidade Federal de Alagoas. Retrieved September 11, 2021, from https://ufal.br/ufal/noticias/2019/11/lapis-alerta-que-mais-um-satelite-detectou-grande-vazamento-de-oleo

Avalbaev, G., & Kadirov, S. (2021). Oil polution problems. Universum: Технические Науки, 11(92).

BBC News Русская служба. (2021, August 11). Разлив нефти под Новороссийском оказался в сотни тысяч раз больше. Что известно. Retrieved September 20, 2021, from https://www.bbc.com/russian/news-58174151

BBC News. (2020, June 9). Russian Arctic oil spill pollutes big lake near Norilsk. Retrieved June 4, 2022, from https://www.bbc.com/news/world-europe-52977740

Bentz, C. M. (2006) Reconhecimento Automático de Eventos Ambientais Costeiros e Oceânicos em Imagens de Radares Orbitais (Thesis). COPPE/UFRJ- Civil engineering program.

Brekke, C., & Solberg, A. H. (2005). Oil spill detection by satellite remote sensing. Remote Sensing of Environment, 95(1), 1–13. https://doi.org/10.1016/j.rse.2004.11.015

Brown, H. M., Bittner, J. P., & Goodman, R. H. (1996). The limits of visibility of spilled oil sheens. Proceedings of the Second Thematic International Airborne Remote Sensing Conference and Exhibition, 3, 327.

Castilho, J. G. (2005, March). Integração de Dados de Métodos Potenciais e de Sensoriamento Remoto Como Subsidio a Exploracao Petrolifera Offshore das bacias de Cumuruxatiba e Jequitinhonha (Master's dissertation). UFRJ/COPPE. http://labsar.lamce.coppe.ufrj.br/pdf/Jose%20Guilherme%20de%20Castilho.pdf

Chaturvedi, S. K., Banerjee, S., & Lele, S. (2020). An assessment of oil spill detection using Sentinel 1 SAR-C images. Journal of Ocean Engineering and Science, 5(2), 116–135. https://doi.org/10.1016/j.joes.2019.09.004

Crisp, D. J. (2004, May). The State-of-the-Art in Ship Detection in Synthetic Aperture Radar Imagery. DSTO Information Sciences Laboratory.

Depellegrin, D., & Pereira, P. (2016). Assessing oil spill sensitivity in unsheltered coastal environments: A case study for Lithuanian-Russian coasts, South-eastern Baltic Sea. Marine Pollution Bulletin, 102(1), 44–57. https://doi.org/10.1016/j.marpolbul.2015.12.005

European Space Agency-b. (n.d.). Sentinel-1 SAR User Guide - Acquisition Modes. Sentinel Online. Retrieved September 20, 2021, from https://sentinels.copernicus.eu/web/sentinel/user-guides/sentinel-1-sar/acq

European Space agency. (n.d.). RUS Training Session. RUS Copernicus. Retrieved August 8, 2021, from https://rus-copernicus.eu/portal/

European Space Agency. (n.d.). Sentinel-1 SAR User Guide. Sentinel Online. Retrieved September 20, 2021, from https://sentinels.copernicus.eu/web/sentinel/user-guides/sentinel-1-sar.

European Space Agency. (n.d.). Sentinel-1. ESA. Retrieved November 5, 2020, from https://sentinel.esa.int/web/sentinel/missions/sentinel-1

Evsukoff, A. G. (2019, December). Ranking de Exsudações de óleo como suporte à exploração petrolífera em águas ultra-profundas: estudo de caso no Golfo do México (Thesis). COPPE/UFRJ- Civil engineering Phd program. http://labsar.lamce.coppe.ufrj.br/pdf/Enrico%20Campos%20Pedroso_D.pdf

Fingas, M. (2016). Oil Spill Science and Technology (2nd ed.). Gulf Professional Publishing.

Fingas, M., & Brown, C. (2014). Review of oil spill remote sensing. Marine Pollution Bulletin, 83(1), 9–23. https://doi.org/10.1016/j.marpolbul.2014.03.059

Garcia, J. G. (1982). Sensoriamento Remoto: Principios E Interpretacao De Imagens. Nobel.

Henderson, F. M., & Lewis, A. J. (1998). Principles and Applications of Imaging Radar (Manual of Remote Sensing, Volume 2) (3rd ed.). Wiley.

Joel MacDonald, MDA Geospatial Services Inc. (2021, May 27). Bubbling Crude And Understanding Seeps. Hart Energy. Retrieved July 20, 2021, from https://www.hartenergy.com/ep/exclusives/bubbling-crude-and-understanding-seeps-29154

Lehner, S., & Tings, B. (2015). MARITIME PRODUCTS USING TERRASAR-X and SENTINEL-1 IMAGERY. The International Archives of the Photogrammetry, Remote Sensing and Spatial Information Sciences, XL-7/W3, 967–973. https://doi.org/10.5194/isprsarchives-xl-7-w3-967-2015

Li, Y., Yu, Q., Xie, M., Zhang, Z., Ma, Z., & Cao, K. (2021). Identifying Oil Spill Types Based on Remotely Sensed Reflectance Spectra and Multiple Machine Learning Algorithms. IEEE Journal of Selected Topics in Applied Earth Observations and Remote Sensing, 14, 9071–9078. https://doi.org/10.1109/jstars.2021.3109951

Macdonald, I. R., Guinasso, N. L., Ackleson, S. G., Amos, J. F., Duckworth, R., Sassen, R., & Brooks, J. M. (1993). Natural oil slicks in the Gulf of Mexico visible from space. Journal of Geophysical Research, 98(C9), 16351. https://doi.org/10.1029/93jc01289

Mityagina, M., & Lavrova, O. (2016). Satellite Survey of Inner Seas: Oil Pollution in the Black and Caspian Seas. Remote Sensing, 8(10), 875. https://doi.org/10.3390/rs8100875

Open Access Hub. (n.d.). Copernicus Open Access Hub. Retrieved June 8, 2020, from https://scihub.copernicus.eu

Packard, N. H., Crutchfield, J. P., Farmer, J. D., & Shaw, R. S. (1980). Geometry from a Time Series. Physical Review Letters, 45(9), 712–716. https://doi.org/10.1103/physrevlett.45.712

Paes, R. L. (2015). Detecção de Alvos na Superfície do Mar Utilizando Imagens SAR Orbitais (Thesis). INPE- Phd in Remote sensing. http://urlib.net/8JMKD3MGP3W34P/3L83TUB

Paradella, W. R., Mura, J. C., Gama, F. F., Santos, A. R., & Silva, G. G. (2015, April). Radares Imageadores (SAR) orbitais: tendências em sistemas e aplicações INPE/Simpósio Brasileiro de Sensoriamento Remoto, 8445–8452.). http://www.dsr.inpe.br/sbsr2015/files/p0506.pdf

Pellon M., F., Marmol, A. M. Q., Pedroso, E. C., Beisl, C. H., Welgan, P., & Morales, L. M. (2004). Analysis of RADARSAT-1 data for offshore monitoring activities in the Cantarell Complex, Gulf of Mexico, using the unsupervised semivariogram textural classifier (USTC). Canadian Journal of Remote Sensing, 30(3), 424–436. https://doi.org/10.5589/m04-019

Pinel, N., Bourlier, C., & Sergievskaya, I. (2010). Unpolarized emissivity of thin oil films over anisotropic Gaussian seas in infrared window regions. Applied Optics, 49(11), 2116. https://doi.org/10.1364/ao.49.002116

Portabella, M. (2022, November). Wind Field Retrieval from Satellite Radar Systems (Thesis). University of Barcelona-program in Astronomy and Meteorology. https://researchgate.net/publication/256474198_Wind_Field_Retrieval_from_Satellite_Radar_Systems

Rebello, V. P. A. (1012, May). Ranking fuzzy de exsudações de óleo detectadas com dados RADARSAT-1 na Bacia de Campos (Master's dissertation). UFRJ/COPPE. http://labsar.lamce.coppe.ufrj.br/pdf/Vitor%20Paiva%20Alcoforado%20Rebello.pdf

Remote Sensing Tutorials. (2019, August 6). Governmant of Canada. Retrieved October 19, 2020, from https://www.nrcan.gc.ca/maps-tools-and-publications/satellite-imagery-and-air-photos/tutorial-fundamentals-remote-sensing/9309

Roriz, C. E. D. (2006, June). Detecção de exsudações de óleo utilizando imagens do satélite RADARSAT-1 na porção offshore do Delta do Níger (Master's dissertation). COPPE/UFRJ-Civil engineering program. http://labsar.lamce.coppe.ufrj.br/pdf/Carlos%20Eduardo%20Dias%20Roriz.pdf

Sabins, F. F. (1996). Remote Sensing: Principles and Interpretations (Third Edition). W. H. Freeman.

Silva, A. F. T. (2008). Identificação de regras de associação interessantes em uma base de dados sobre exsudações de óleo no golfo do México (Master's dissertation). COPPE/UFRJ – Civil engineering program.

Silva, G.M.A. (2013) Uso da dimensão fractal dinâmica para caracterização de manchas de óleo no mar a partir da análise de imagens SAR (thesis). Tese de doutorado. COPPE/UFRJ-Civil engineering program.

Silva, G.M.A.; Miranda, F.P.; Vieira, J.A. e Rocha, A.C. (2019). Detecção e caracterização de alvos na imagem RADARSAT-1 da superfície do mar no Golfo do México utilizando diagramas de espaço de estados defasados. INPE/Simpósio Brasileiro de Sensoriamento Remoto, 2184-2187.

Song, D., Zhen, Z., Wang, B., Li, X., Gao, L., Wang, N., Xie, T., & Zhang, T. (2020). A Novel Marine Oil Spillage Identification Scheme Based on Convolution Neural Network Feature Extraction From Fully Polarimetric SAR Imagery. IEEE Access, 8, 59801–59820. https://doi.org/10.1109/access.2020.2979219

Staples, J., & Rodrigues, D. F. (2013, April). Maritime environmental surveillance with RADARSAT-2. INPE/Simpósio Brasileiro de Sensoriamento Remoto, 8445–8452. http://marte2.sid.inpe.br/col/dpi.inpe.br/marte2/2013/05.29.00.21.34/doc/p1061.pdf

Teoria : Sistemas de Radar. (2016). DPI-INPE. Retrieved August 19, 2020, from http://www.dpi.inpe.br/spring/teoria/radar/radar.htm

Ulaby, F. T., Moore, R. K., & Fung, A. K. (1986). Microwave Remote Sensing: Active and Passive, Volume I: Fundamentals and Radiometry (Vol. 1). Artech House Publishers.

Unwin, D. J., & Hepple, L. W. (1974). The Statistical Analysis of Spatial Series. The Statistician, 23(3/4), 211. https://doi.org/10.2307/2987581

Vachon, P.W., & Wolfe, J. (2008). GMES Sentinel-1 Analysis of Marine Applications Potential (AMAP).